Magyarhoni Földtani Társulat
Földtani Közlöny
Hungarian Geological Society

156/3, 303–321., Budapest, 2026

DOI: 10.23928/foldt.kozl.2026.156.3.303

From invisible gold in arsenian pyrite to gold-rich brown "muds" in karst cavities: supergene Au–Ag remobilisation in the Bigar area, Western Timok, Serbia

MAGYAR, Levente M.[1,*]; MÁRTON, István[2]; ZDRAVKOVIĆ, Mladen[2]; PAPP, Richárd Z.[1]; WEISZBURG, Tamás[3]; HARMAN-TÓTH, Erzsébet[4]

[1]Unexmin Georobotics Ltd., Budapest, Hungary
[2]DPM Metals Inc., Bor, Serbia
[3]Department of Mineralogy, Institute of Geography and Earth Sciences, Eötvös Loránd University, Budapest, Hungary
[4]Eötvös Museum of Natural History, Eötvös Loránd University, Budapest, Hungary

*mlevente89@gmail.com

Az arzénes pirit láthatatlan aranyától az aranyban gazdag, barna karsztkitöltésekig: szupergén Au–Ag remobilizáció a Bigar területen, Nyugat-Timok, Szerbia

Összefoglalás

A szerbiai Timoki Magmás Komplexum északnyugati részén, a Bigar–Korkan terület karbonátos kőzeteiben barna, földes-agyagos karsztkitöltések fordulnak elő, amelyek aranytartalma helyenként meghaladja a 10 ppm-et. Elsősorban a Bigar területről származó minták terepi, ásványtani, szemcseméret-eloszlási, elektronmikroszkópos és mikroszondás adatait értékeltük az aranyhordozó fázisok azonosítása és a képződési folyamatok rekonstruálása érdekében. A vizsgált barna „sár" egy agyagdús összlet, mely törmelékes szilikátok, másodlagos Pb–Mn-fázisok és pirit utáni, Fe-oxid/oxihidroxid pszeudomorfózák heterogén keveréke. A szögletes és lekerekített szemcsék, a koncentrikus goethit–agyag bevonatok és a rétegzéssel párhuzamos, Fe-dús kiválások áthalmozott szemcsék és későbbi ásványkiválások együttes jelenlétére utalnak. A termésarany, az elektrum és az Au–Ag-szulfid főként e pszeudomorfózák belsejében jelenik meg, míg porózus külső részeik gyakran nemesfémekben szegényebbek. Az elemzett, Au-dús Au–Ag-szulfid összetétele petrovskaite-szerű, de biztos ásványfaji azonosítása nem lehetséges. A javasolt modell szerint a kezdeti, üde As-tartalmú piritek feltételezett láthatatlan aranyát szulfidoxidáció, majd karbonáttal pufferelt közegben rövid távú, tioszulfát által segített Au–Ag-remobilizáció követte. A karbonátoldódás felszabadította az ellenálló, aranytartalmú pszeudomorfózákat, amelyek karsztüregekbe szállítódtak és ott feldúsultak. A karsztvízszint ingadozásai változtathatták az oxigénellátást: a vízszintsüllyedés elősegíthette az oxidációt, míg a vízzel telített, korlátozott vízcseréjű üregekben az oxigén elfogyása helyi reduktív viszonyok kialakulásához vezethetett. Oldott szulfid jelenlétében ezek a körülmények késői Au–Ag-, Ag- és Ag–Hg-szulfidképződésnek kedvezhettek. Az újbóli oxidáció a külső szemcseövek szulfidjainak elbontását okozhatta. A kimagasló aranytartalmak ezért a kémiai remobilizáció, a meddő karbonát eltávolítása és az aranyhordozó szemcsék karsztcsapdákban történő fizikai koncentrációjának együttes eredménye. Mindezek alapján a karsztosodott, szulfidtartalmú karbonátos kőzetek Fe-oxid/oxihidroxid-szemcséket tartalmazó üregkitöltései további aranykutatásra érdemes célpontok lehetnek, melyek kutatását geokémiai, geofizikai és távérzékelési módszerek tovább segíthetik.

Tárgyszavak: karsztos áthalmozódás; goethit–hematit pszeudomorfóza; szulfidoxidáció; redoxváltozások; másodlagos ásványképződés; petrovskaite

Abstract

In the northwestern part of the Timok Magmatic Complex, Serbia, brown, earthy–clayey karst-infill materials occur within the carbonate rocks of the Bigar–Korkan area, with gold contents locally exceeding 10 ppm. Field observations, mineralogy, grain-size distribution, electron microscopy, and electron microprobe data from samples collected mainly in the Bigar area were evaluated together to reconstruct their paragenetic evolution. The studied brown "mud" is a clay-rich assemblage consisting of a heterogeneous mixture of detrital silicates, secondary Pb–Mn phases, and angular to rounded Fe oxide/oxyhydroxide pseudomorphs after pyrite. Angular and rounded grains, concentric goethite–clay coatings and layer-parallel Fe-rich precipitates suggest the coexistence of reworked grains and later mineral precipitates. Native gold, electrum, and Au–Ag sulphide occur mainly in the inner parts of these pseudomorphs, whereas their porous outer parts are commonly depleted in precious metals. The analysed Au-rich Au–Ag sulphide has a petrovskaite-like composition, but its mineral species cannot be identified with certainty. According to the proposed model, the inferred invisible gold in the initial, fresh As-bearing pyrite was followed by sulphide oxidation and then by short-range, thiosulphate-assisted Au–Ag

remobilisation in a carbonate-buffered environment. Carbonate dissolution liberated the resistant, gold-bearing pseudomorphs, which were transported into karst cavities and concentrated there. Fluctuations in the karst water table may have changed oxygen availability: falling water levels likely promoted oxidation, whereas oxygen depletion in water-filled cavities with restricted water exchange likely led to the development of locally reducing conditions. In the presence of dissolved sulphide, these conditions may have favoured late precipitation of Au–Ag, Ag, and Ag–Hg sulphides. Renewed oxidation likely caused the breakdown of sulphide minerals in the outer grain zones. The exceptionally high gold contents are therefore the combined result of chemical remobilisation, removal of barren carbonate, and physical concentration of gold-bearing grains in karst traps. These findings suggest that karst infills containing Fe oxide/oxyhydroxide grains should be considered potential gold exploration targets where karstification affects sulphide-bearing carbonate rocks. Exploration for such accumulations may be supported by geochemical, geophysical and remote-sensing methods.

Keywords: karstic redeposition; goethite–hematite pseudomorph; sulphide oxidation; redox fluctuations; secondary mineral formation; petrovskaite

Introduction

Brown, earthy to clayey, weakly consolidated materials are common products of weathering in carbonate-hosted ore systems, but their origin is often difficult to define. In the field such materials may look similar, even if they formed by different processes. They may represent residual products left behind after carbonate dissolution, detrital material transported into cavities, authigenic precipitates formed during oxidation, or mixed karst-infill material. This ambiguity is particularly important where these materials contain anomalously high gold grades, because their metal content cannot be explained based on field appearance alone. Accordingly, this study aims not only to clarify the origin and evolution of the brown materials, but also to constrain the source, mineralogical hosts, and redistribution of Au and associated elements. Establishing these relationships is relevant to mineral exploration because distinguishing primary hydrothermal mineralisation from supergene redistribution may improve the prediction of the location and continuity of mineralised material.

The Bigar area, in the northwestern Timok Magmatic Complex in Eastern Serbia, is a good example of this problem. Brown mud-like material was observed in exploration trenches and drill cores within limestone-, marble- and calc-silicate-dominated settings of the Bigar and Korkan exploration areas. Exploration geochemistry datasets showed that some of these materials contain unusually high Au, together with Ag, Pb, Zn, Mn and As anomalies. These results raised questions about the minerals hosting the gold and the processes responsible for its concentration.

Previous regional studies described the main mineralisation types and their geological setting. Petrographic and mineralogical observations of the brown "muds" were reported in the first author's MSc thesis together with subsequent company studies, and some results were summarised in company technical reports. The present paper brings these investigations together in a detailed study focused on the brown karst infills. By combining mineral-chemical analyses, textural observations and size-fraction Au assays, it documents the gold-bearing phases and their host grains and examines the evidence for alteration and redeposition.

The aim of this paper is to use these observations to develop a mineralogical and paragenetic model for the formation of Au-rich brown "muds" (often above 4–5 ppm Au), based mainly on samples from the Bigar area. Additional samples from Korkan and Korkan West-Bigar Hill are used only where they help to identify the original sulphide assemblages and transitional oxidation products. The study focuses on the textural position of Au-bearing phases, their host minerals, and the relationship between pyrite-derived Fe oxide/oxyhydroxide pseudomorphs, clay-rich domains and karst-related redeposition. The working hypothesis is that the brown "muds" are composite supergene-karstic products formed by sulphide oxidation, short-distance Au–Ag remobilisation, and physical redeposition of Au-bearing Fe oxyhydroxide grains. Processes such as thiosulphate complexing, Au–Ag sulphide formation and redox fluctuation are considered in this framework and will be discussed in detail following the presented mineralogical observations.

Geological and exploration background

Regional geological and metallogenic setting

The Bigar and Korkan areas are located in the northwestern part of the Timok Magmatic Complex (TMC) in eastern Serbia. The TMC belongs to the Apuseni–Banat–Timok–Srednogorie belt (*Figure 1*) within the broader Alpine–Balkan–Carpathian–Dinaride metallogenic province of the Tethyan orogenic system (JANKOVIĆ 1997, HEINRICH & NEUBAUER 2002). This belt is known mainly for Late Cretaceous magmatic-hydrothermal systems, including porphyry Cu–Au, polymetallic skarn and carbonate-replacement, high-sulphidation epithermal Cu–Au and distal sedimentary rock-hosted Au mineralisation (ZIMMERMAN et al. 2008, KNAAK et al. 2016). At the NW part of TMC, approximately 25 km northwest of Bor, a distinct gold mineralisation dominantly hosted by calcareous sedimentary rocks has been outlined at Bigar Hill, Korkan, Korkan West and Kraku Pešter prospect areas (VAN DER TOORN et al. 2013, KNAAK et al. 2016, DE WEERDT et al. 2021).

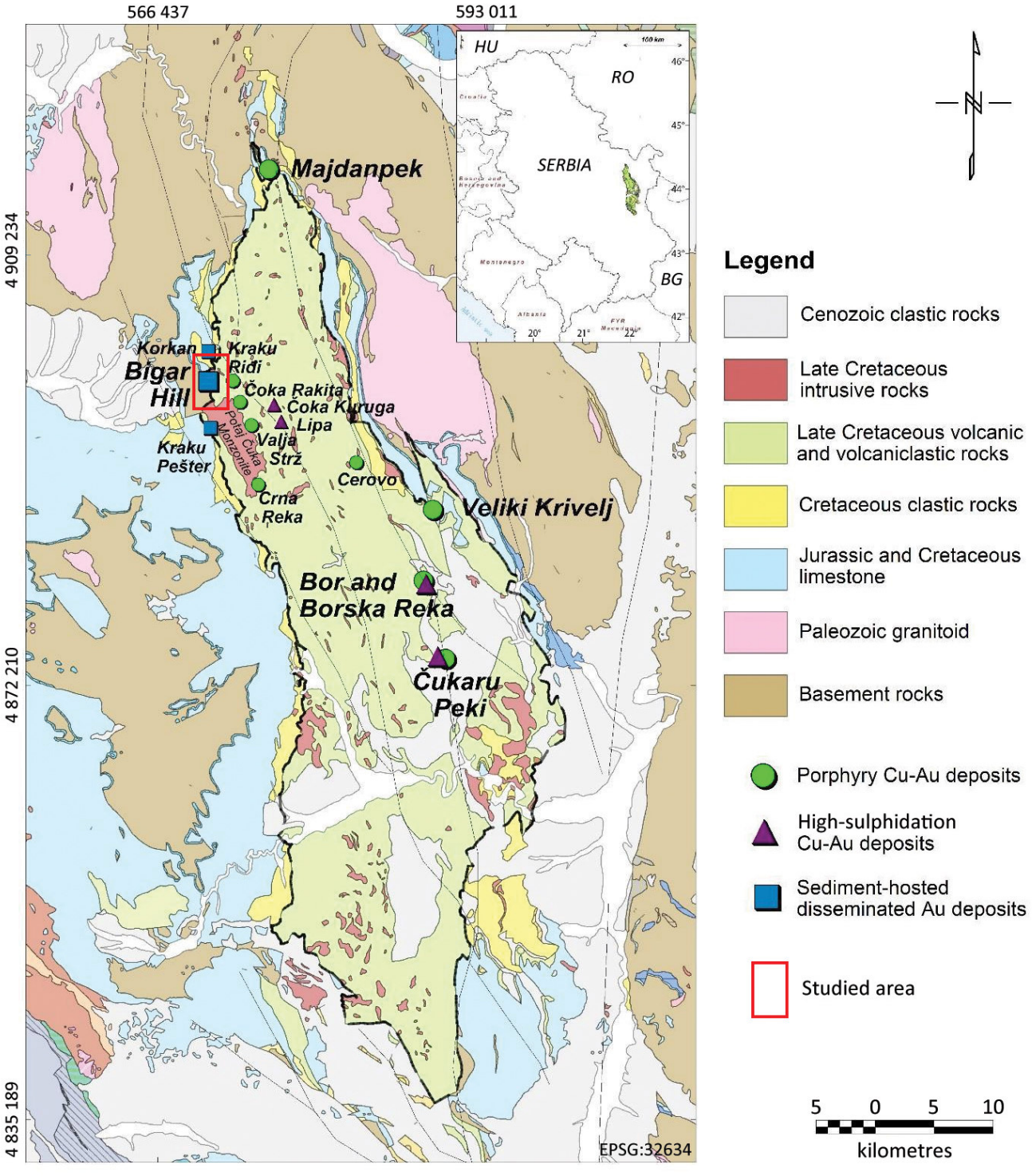


Figure 1. Simplified geological map of the Timok Magmatic Complex showing the principal ore deposits and the studied area, modified after MÁRTON et al. (2026, fig 6)

1. ábra. *A Timoki Magmás Komplexum egyszerűsített földtani térképe a főbb érctelepek és a vizsgált terület feltüntetésével, MÁRTON et al. (2026) 6. ábrája alapján, módosítva*

Exploration history and recent discoveries

The first phase of modern gold exploration at the NW part of TMC took place between 2004 and 2009 with soil sampling, trenching, geophysical surveys and limited diamond drilling mostly focusing on porphyry and high-sulphidation type mineralisation. Between 2010 and 2013, Avala Resources Ltd. focused exploration on carbonate sequences, where drilling and surface sampling outlined sedimentary rock-hosted gold mineralisation at Bigar Hill, Korkan and Kraku Pešter prospects (VAN DER TOORN et al. 2013, KNAAK et al. 2016). After 2016, the exploration activity focused on

shallow oxide mineralisations and led to the discovery of the Korkan West prospect. In 2020 DPM Metals published an updated mineral resource estimate and a prefeasibility study for these sedimentary rock-hosted gold deposits, which outlined a total of 32.3 Mt of ore at 1.27 g/t Au grade (1.319 Moz total contained gold) indicated mineral resource, from which 8.2 Mt being identified as oxide ore (DE WEERDT et al. 2021). Discoveries announced since 2023 include the Čoka Rakita gold-skarn deposit and deeper Cu–Au-polymetallic skarn and carbonate-replacement mineralisation at Dumitru Potok, Frasen and Rakita North (IVASCANU 2024, ZDRAVKOVIĆ et al. 2024, ŽIVANOVIĆ et al. 2024, DPM METALS 2026, MILIĆ et al. 2026). These discoveries illustrate the diversity of primary mineralisation in the region. The findings of the present study may help guide exploration around these prospects for shallow, gold-rich, oxidised karst fills, where near-surface mineralisation has undergone weathering followed by physical reworking of its weathering products in a karstic environment.

Local stratigraphy, magmatism and karstification

The local stratigraphy of the studied area is dominated by Jurassic and Lower Cretaceous carbonate rocks, overlain by Cretaceous clastic, volcaniclastic and marl units (*Figure 2*). The older carbonate sequence includes Jurassic limestone (JLS) and Lower Cretaceous limestone (KLS), the latter commonly containing black chert. Above this carbonate basement, the Albian–Cenomanian succession includes basal breccias and calcareous siliciclastic rocks grouped into the S1 unit. The basal breccias are interpreted to originate partly as fills of early karst features along the erosional unconformity, with additional contributions from fault-slip and debris-flow deposits (KNAAK et al. 2016). These Albian–Cenomanian clastics are overlain by volcanic-detrital sandstones and related clastic rocks of the S2 unit, and by the Santonian marl unit (SMR). Andesitic volcaniclastic and epiclastic rocks occur higher in the sequence or as intrusive subvolcanic bodies (VAN DER TOORN et al. 2013, KNAAK et al. 2016, ŽIVANOVIĆ 2019). A large north-northwesterly oriented monzonitic pluton (Potaj Čuka monzonite) and numerous dioritic stocks, dykes, and sill-like intrusions were mapped at NW Timok. These intrusions were emplaced during a Late Cretaceous magmatic activity between approximately 84 and 78 Ma, and are generally younger than the 89–83 Ma old magmatism in the eastern part of TMC (KOLB et al. 2013, KNAAK et al. 2016).

Karstification is mainly observed along the unconformable contact between the Jurassic–Lower Cretaceous limestones and the overlying S1 unit. KNAAK et al. (2016) described locally missing carbonate intervals, karst features along NW- and NE-trending fractures, and cavities filled by red-brown, Fe-rich sandstone and siltstone. At Bigar Hill, enlarged fractures, collapsed caves and sinkholes, terra rossa, laminated cave fills and local basal breccias were also observed (ŽIVANOVIĆ, 2019). These features suggest that karstification developed along pre-existing faults and fractures during exposure and erosion of the carbonate rocks, before S1 deposition. The resulting cavities were subsequently filled with breccia and siliciclastic material associated with the S1 and S2 units, before the main hydrothermal gold mineralisation. The locally high porosity and permeability of these early fills and the surrounding fractured limestone provided favourable pathways for mineralising fluids. Some of these fills were, therefore, mineralised during the primary hydrothermal event and form an important part of the Bigar Hill deposit. The lower mineralised horizon follows the limestone and S1 sandstone contact, where gold-bearing pyrite occurs in decarbonated clastic rocks and Fe-rich karst infill. Hydrothermal carbonate dissolution further increased porosity and facilitated fluid flow, sulphide formation and gold precipitation (KNAAK et al. 2016, ŽIVANOVIĆ 2019). Following mineralisation, Cenozoic faulting modified the distribution and preservation of the deposits. NW-trending faults displaced the Korkan mineralisation, while younger E to E-NE-trending normal faults bounded the downthrown Bigar Hill graben during early Miocene extension (KNAAK et al. 2016). Differential block movement may have contributed to the local exposure of mineralised rocks. Where sulphide-bearing rocks were exposed to meteoric waters, pyrite was replaced by goethite and hematite, and – when being liberated from their host rock – the Fe oxide/oxyhydroxide grains and brown clay-rich material were locally transported into karst cavities. Limited remobilisation of Au and Ag might also have occurred during this stage. Although karstification may still be ongoing, the proposed history includes early karstification and sedimentary infilling before mineralisation; hydrothermal carbonate dissolution during sulphide mineralisation; and later supergene weathering and karst-related reworking. The studied brown "muds" are interpreted to record this later weathering and reworking, together with local mineral precipitation.

Gold mineralisation in the studied area

Within this karst-influenced stratigraphic and structural setting, the sandstone-hosted Au mineralisation of Bigar Hill is mainly related to sulphidation of reactive Fe-bearing components and carbonate cement in the S1 and S2 units (PAČEVSKI 2012a, b; ŽIVANOVIĆ 2019). It can be considered a Carlin-type gold mineralisation related mainly to lithological boundaries and structural units, showing average grades of 1–2 ppm Au. Pyrite occurs in calcite or dolomite cement, stylolites, fractures and micro-fractures, and may replace Fe-bearing aluminosilicates and carbonate grains. Gold in this assemblage is mostly "invisible", occurring as structurally bound Au or submicrometre native gold in pyrite and arsenic-rich pyrite (RADTKE et al. 1980; HOFSTRA & CLINE 2000; CLINE et al. 2005; MUNTEAN et al. 2011; PAČEVSKI 2012a, b; ŽIVANOVIĆ 2019).

The Bigar area is situated south-southeast of Bigar Hill, between Bigar Hill and the Late Cretaceous Potaj Čuka monzonite intrusion (*Figure 2*). The thermal effect of magmatic

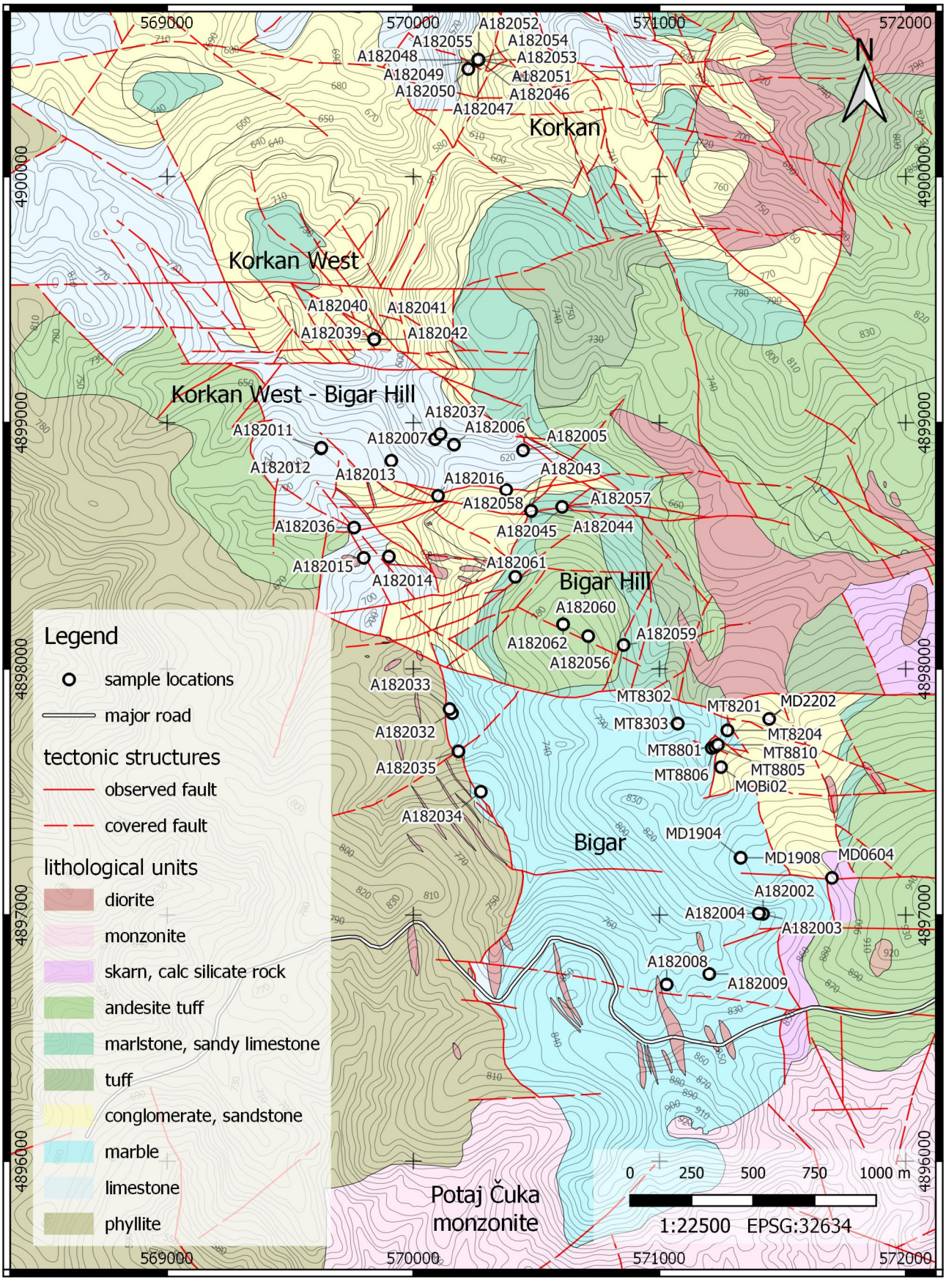


Figure 2. Local geological map of the studied area compiled from GIS data supplied by DPM Metals (unpublished company data) with the location of the collected samples

2. ábra. *A vizsgált terület földtani térképe a DPM Metals által rendelkezésünkre bocsátott, nem publikált vállalati GIS-adatok alapján, valamint a gyűjtött minták helyei*

intrusions is expressed by recrystallisation of limestone into marble or crystalline limestone, and locally by calc-silicate/skarn assemblages. The brown, muddy karst-infill material with high Au grades is found in the karstic cavities of the carbonate rocks. This karst-infill material is also present in drillholes of the area as deep as 119–134 m, with Au grades up to 11.77 ppm. These sample types of the Bigar area make it suitable for studying the process of gold mineralisation developed in carbonate rocks within the broader Bigar Hill–Korkan-Korkan West exploration system.

Sample material and analytical methods

The material used in this paper derives from three stages of the first author's work in the Bigar–Korkan area: an MSc study in 2014, a field mapping of limestone-dominated areas in 2017, and a petrographic study of oxide and transitional ores in 2018. Field access, sampling and the use of exploration drill core samples were made possible by Avala Resources Ltd., the company that conducted geological exploration at that time. Since then, the project has become part of DPM Metals portfolio through its local subsidiary. The project area is included in DPM Metals prefeasibility study, which is presented in a public NI 43-101 report (DE WEERDT et al. 2021).

The 2014 work included 62 collected samples, of which 44 were considered to be genetically related to the brown weathering products, including 21 drill-core samples, 21 trench samples and two outcrop samples (*Figure 2*). In this study, ten carbonate-rich bulk samples were treated in 10% HCl, 13 samples were sieved and 88 XRD analyses were carried out to determine the main mineral constituents of bulk samples and separated grain-size or colour fractions. In total, 21 polished sections and grain mounts were studied by SEM–EDX focusing on the textural position of precious-metal phases and their relation to goethite-hematite grains, clay-rich domains and carbonate or calc-silicate host rocks. One Au-bearing grain was analysed by SEM–WDX, and selected sulphides and Fe oxyhydroxides from three samples were checked by Raman spectroscopy. Results of this study form part of a publicly accessible MSc thesis at ELTE, Budapest (MAGYAR 2014).

During and following a detailed mapping campaign in 2017 and 2018, further 45 oxide and transitional samples were selected from the Bigar, Bigar Hill, Korkan West-Bigar Hill, Korkan West and Korkan areas (*Figure 2*). These samples were studied by reflected light microscopy, SEM–EDX and, for selected areas, EMPA–WDS/EDS mapping. The latter methods were used to document Au-, Ag-, As-, S-, Fe-, Pb-, Zn-, Mn-, Ti- and P-bearing microdomains, especially in pyrite-derived Fe oxyhydroxide pseudomorphs and karst-related infill materials. The studied samples were selected to represent key textural stages, not to provide a statistically representative sample population. The results of the 2017–2018 sampling campaigns were presented in DPM Metals internal report (MAGYAR 2018).

The SEM–EDX instrument used in this study is an AMRAY 1830 SEM equipped with an EDAX PV9800 EDS detector (Electron Microanalysis Laboratory, Department of Petrology and Geochemistry, Eötvös Loránd University, Budapest, Hungary). This instrument has digital imaging and analysis system (Tescan Satellite 1130 and Moran Scientific QXAS QUOLL EPP). Analysis conditions were 20kV acceleration voltage, 1 nA beam current, focused electron beam (~50 nm in diameter) and the measuring time was 100 sec (live time).

The EMPA–WDS/EDS instrument is a JEOL-JXA 8600 microprobe upgraded with a SAMX control system used on 20 kV acceleration voltage and 20 nA beam current (Institute of Mineralogy–Geology, University of Miskolc, Hungary.)

The XRD instrument is a Siemens D5000 diffractometer with Bragg-Brentano geometry, equipped with secondary pyrolytic graphite monochromator, using Cu-Kα radiation (Department of Mineralogy at Eötvös Loránd University Budapest, Hungary). Counting time was 2 seconds and step size was 0.05ş for routine analyses. In some cases, where routine analytical conditions yielded poor quality patterns (due to small grain sizes or composite mixtures), measurements were repeated with longer counting time and larger steps (7 sec counting time per 0.1°), in order to improve signal-to-noise ratio and enable more precise evaluation. The data were evaluated with Bruker's EVA software.

Raman spectroscopy was carried out by a HORIBA JobinYvon LabRAM HR type dispersive Raman microspectrometer, equipped with an Olympus BXFM light microscope and a thermoelectrically cooled CCD detector (ELTE Faculty of Science Research and Instrument Core Facility). Samples were excited by a 532 nm wavelength green laser beam, and a 600 grooves/mm grating and a 100× (numerical aperture 0.9) objective were used. Calibration of the instrument was done by monitoring the Rayleigh line (0 cm^{-1} Raman shift).

Gold grade values that were used to guide the 2014 sample selection were obtained from routine Avala Resources analyses of drill-core and trench-channel intervals. The analyses were carried out in the laboratory of SGS Serbia, Bor. Gold in samples of the 2014 study was analysed by fire assay with AAS finish, while 50 other elements were analysed by AAS or ICP–MS following a two-acid digestion. Company sample analysis standards changed in 2016, so the samples of the 2018 study were digested by near-total four-acid (HF–HNO_3–$HClO_4$–HCl) solution prior to the AAS or ICP–MS analyses for 49 elements (DE WEERDT et al. 2021).

The present paper summarises the previous results, focusing mainly on karst-infill materials, carbonate-replacement ores, skarn and marble samples from the Bigar area, with a few mineralised sandstone and transitional samples also used for comparison. When selecting samples one of the main goals was to reveal the paragenesis of the high Au grade karst-infill material; therefore, samples with high Au values (often above 4–5 ppm Au, in some cases even 11.77 ppm Au) were of particular interest.

Several limitations must be considered. Many Au-bearing phases are only a few micrometres in size, so even where they were not observed in a polished section, it does not necessarily imply their absence from the bulk sample. SEM–EDX element overlaps, especially As–Mg, Ca–Sb and S–Hg–Pb, were treated with caution. Most reported Au grades used in this paper are based on company exploration assays. In the 2014 MSc work, 19 selected bulk or separated samples were additionally analysed at the SGS Serbia laboratory in Bor by ICP–MS and AAS for Au and 50 additional elements (MAGYAR 2014). Reported Au grades used for sample selection generally refer to regular exploration intervals, and are not always directly representative of the analysed subsamples presented in this work.

Sample locations, material types and descriptions are provided in *Supplementary Table S1*. The analyses performed on individual samples and separated fractions are listed in Supplementary Table S2. Chemical analytical results and analytical limits are presented in *Supplementary Tables S3a–S3d*.

Results

Au-bearing Fe oxyhydroxide pseudomorphs and brown "muds"

The brown "mud" samples are poorly consolidated, rich in dark brown clay and ochre and brown Fe oxyhydroxides, and generally poor in carbonate content. They occur both in trench exposures (*Figure 3*) and in drill cores (*Figure 4*) in the Bigar and Korkan West-Bigar Hill areas. In trench exposures, they commonly occupy cavities in karstic marble and limestone bodies or occur on their surface. They are generally heterogeneous at hand-specimen and microscopic scale, ranging from banded clay-rich material to chaotic mixtures of Fe oxyhydroxide grains, carbonate fragments and detrital silicate minerals. These samples are characterised by elevated As contents, commonly in the 500–2200 ppm range, together with variable Au, Ag, Pb, Mn, Sb, Cd and Fe contents (*Supplementary Table S3a*). This geochemical character is consistent with the abundance of As- and Pb-bearing Fe oxyhydroxides, Mn–Pb oxyhydroxides and locally precious-metal-bearing Fe oxyhydroxide pseudomorphs observed in polished sections.

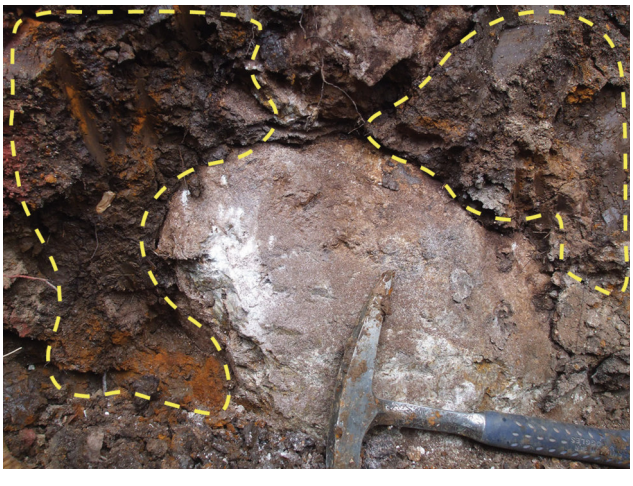


Figure 3. Brown "mud" on karstic marble surface in exploration trench BITR082 (at 58.6 m) outlined with yellow, dashed contour

3. ábra. *Barna „sár" (szaggatott, sárga körvonallal jelölve) a BITR082-es kutatóárok 58,6 m-énél kibukkanó karsztos márvány felszínén*

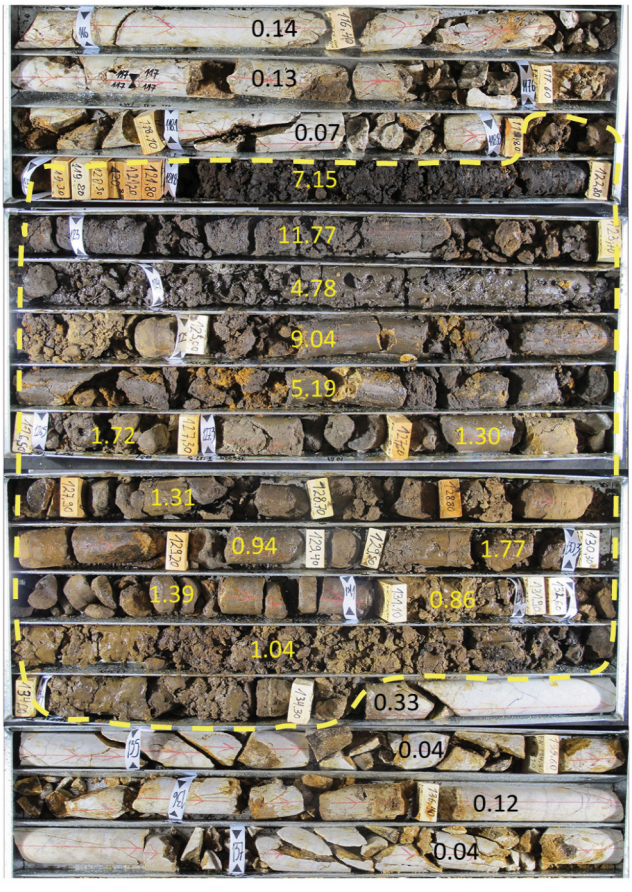


Figure 4. Brown "muds" in drill core BIDD019 outlined with yellow, dashed contour, and with ppm Au grades (yellow and black typed digits). Top left is at 116 m, and bottom right is at 137.5 m depth. (DPM Metals core photo)

4. ábra. *Barna „sár" a BIDD019 fúrómag anyagában, szaggatott, sárga körvonallal jelölve. A ppm-ben megadott Au értékek sárgával és feketével jelölve. Bal felső sarok 116 m, jobb alsó sarok 137,5 m mélységből. (DPM Metals magláda fotó)*

The richest gold-bearing material studied from the Bigar area is represented by a more than 10-m-thick, brown, earthy to clay-rich brown "mud" between marble units in drill hole BIDD019 (*Figure 4*). (The total drilled length in this unit is 15.5 m, but only 10.5 m of brown "mud" was recovered.) Drill core sample MD1908, taken from the 123.5–123.6 m interval, belongs to this group and the corresponding 1 m interval contained 11.77 ppm Au. The same drill hole contains other Au-rich brown "mud" intervals, including 7.15 ppm Au at 122.6–122.7 m and 9.04 ppm Au at 125.6–125.7 m. Macroscopically, these materials are weakly consolidated brown to dark brown sediments, locally banded or brecciated, and rich in rusty brown Fe oxyhydroxide grains (*Figure 5*). Some polished sections show coherent clay-rich domains, whereas others contain angular to subrounded goethite-hematite clasts and detrital grains (*Figures 6; 7/A*).



Figure 5. Fe oxide/oxyhydroxide grains from Au-rich brown "muds", including cube-like grains with variably rounded edges and corners. The sample is the sieved 250-500 µm fraction of MD1908 sample (from drill hole BIDD019)

5. ábra. *Nagy aranytartalmú barna „sárból" szeparált Fe-oxid/oxihidroxid-szemcsék, köztük különböző mértékben lekerekített élű és sarkú, kockaszerű szemcsék. A minta az MD1908-as minta szitált, 250-500 µm-es frakciója (a BIDD019-es fúrásból)*

The brown "muds" are mineralogically mixed. XRD measurements on different colour and separated grainsize fractions identified that clay-rich bands contain smectite, kaolinite and illite. In these assemblages there are also secondary Pb phases such as cerussite needles (*Figure 7/A*) and pyromorphite (*Figure 7/B*). Other domains are richer in goethite–hematite grains, many of which preserve rectangular, pentagonal or rounded shapes (*Figure 7/B*). These grains are interpreted as pseudomorphs after pyrite. Detrital domains contain quartz, K-feldspar, plagioclase, grossular, epidote and locally spinel or other resistant minerals (*Figure 7/A*). Mn–Pb–Fe–Zn oxyhydroxides occur as separate precipitates in vugs.

SEM observations show that Fe oxyhydroxides occur in several textural positions in brown "muds". Some occur as discrete grains with angular to subrounded outlines, suggesting different transport distances during re-deposition (*Figure 7/B*). Others form concentric coatings on detrital grains of quartz and Fe oxyhydroxides, usually with different chemical compositions from the enclosed Fe oxyhydroxide grains (*Figure 7/D*). Goethite-rich domains also occur parallel to layering in the fine-grained, clay-rich parts of the material.

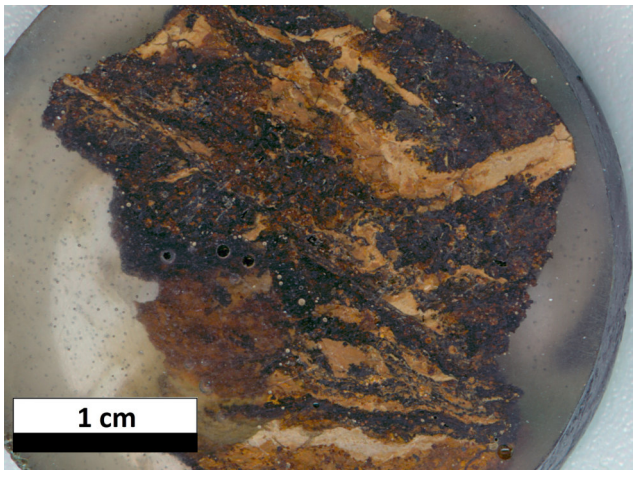


Figure 6. Banded internal macrostructure of the cut and polished MD1902 sample, containing 7.15 ppm Au

6. ábra. *A vágott és polírozott MD1902 minta (7,15 ppm Au) sávos belső makroszerkezete*

The internal textures of the Fe oxyhydroxide grains are also variable. Several grains contain a dense Fe-rich core, commonly hematite-rich, surrounded by a more porous goethite-rich cortex mixed with clay minerals (*Figure 7/E*). Relict sulphides may occur in the core or along internal zones (*Figure 7/C*). In grains that were transported longer distances, the outermost surface may be rounded and coated by an additional goethite–clay mixture (*Figure 7/D*). This structure is important because precious-metal phases are not evenly distributed in the grains. Au–Ag sulphides and electrum occur mostly in the inner domains of goethite-hematite grains, whereas the porous outer cortices are typically poor in these phases (*Figure 7/D*). One concentric Fe oxide grain contains a spongy, approximately 30 µm Au–Ag sulphide aggregate and 2 µm electrum grains near its centre (*Figure 7/F*).

The observed gold-bearing phases in the brown "muds" are native gold, electrum and Au–Ag sulphides. They usually occur in micrometre-sized blebs or irregular patches within Fe oxyhydroxide grains. Ag-bearing phases include acanthite and Ag–Hg sulphides, localised along fracture networks in Fe oxide/oxyhydroxide pseudomorphs after pyrite, often in the vicinity of residual pyrite (*Figure 8/A*). SEM–WDX analysis of the spongy Au–Ag sulphide grain from sample MD1908 showed that SEM–EDX underestimated sulphur in this phase, but confirmed the Au–Ag–S character of the grain (*Figure 7/F; Table I*).

Sieving followed by the analyses of the different grainsize fractions showed that 60–70 wt% of the brown "muds" is composed of <32 µm fraction and around 15 wt% is made up of the 63-125 µm sized fraction, latter being characteristic for the goethite pseudomorphs after pyrite. In sample MD1908, the bulk subsample yielded 18.79 ppm Au, the <32 µm fraction only 2.80 ppm Au, while the 63–125 µm fraction yielded 16.11 ppm Au (*Supplementary Table S3a*). Nevertheless, only two of the six size fractions were analysed for Au. The higher grade of the separately analysed bulk subsample may reflect Au enrichment in one or more unanalysed fractions and/or heterogeneity between subsamples. The highest-grade fraction cannot be identified from the available data, but the results support the importance of coarser Fe oxyhydroxide grains.

Other karst-related samples show similar but lower-grade features. Sample A182015 from the Bigar area is a yellowish-brown, carbonate-rich karst infill from channel BICH133, with 0.94 ppm Au. It contains white, angular to subangular carbonate clasts, grey quartz fragments, orange limonite crusts, black shiny cubes and a clay-rich matrix. Native gold

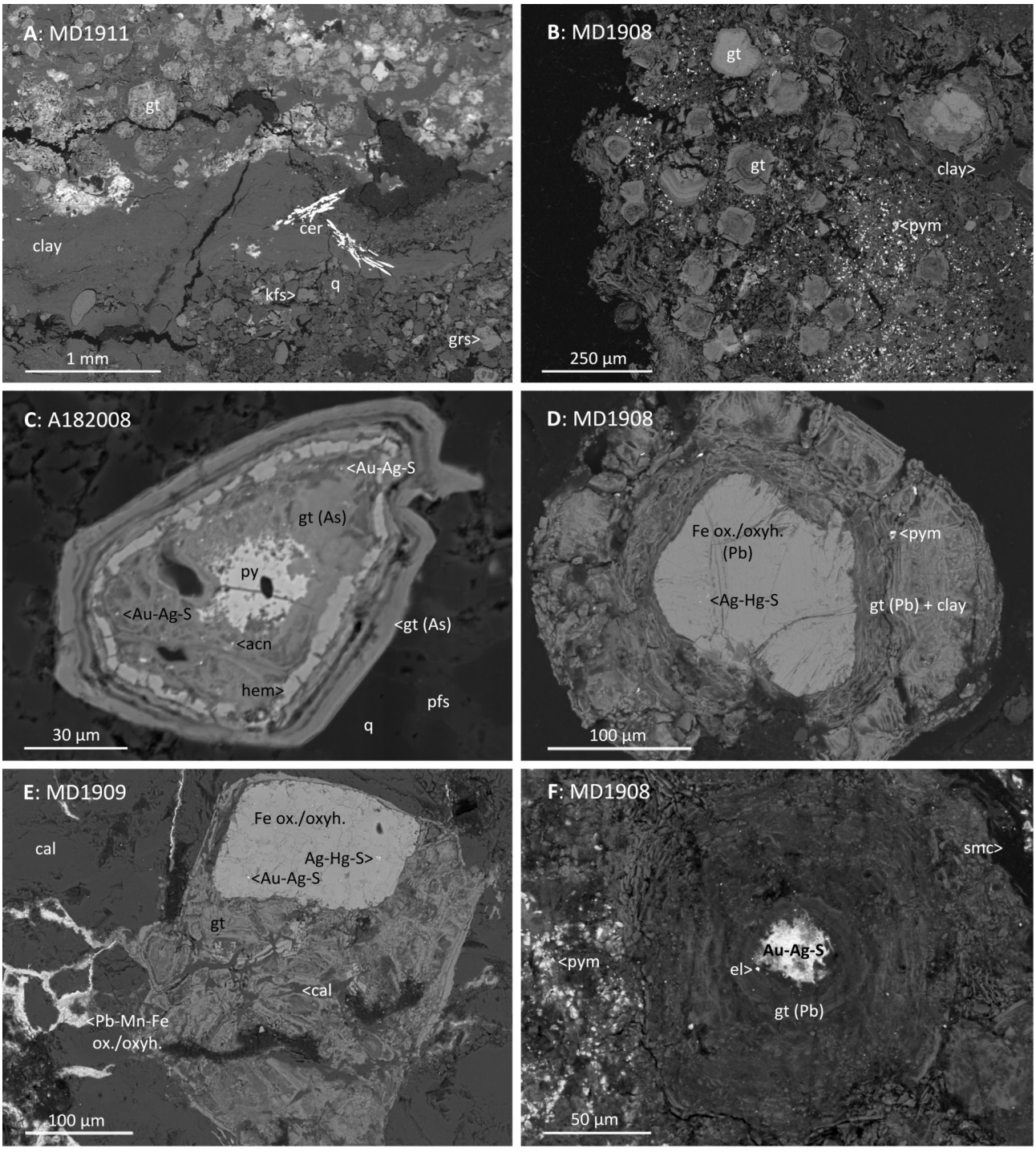


Figure 7. BSE images of SEM-EDS/WDS analyses (at an accelerating voltage of 20 kV) of the textures of brown "mud" ores and genetically related rocks. A) Banded internal microstructure of a brown "mud" with goethite (gt) pseudomorph-rich, clay-dominated and detrital-rich parts with quartz (q), K-feldspar (kfs), grossular (grs). B) Grainy internal microstructure of a brown "mud" sample with pyromorphite (pym). C) From a skarn: pentagonal concentric goethite (gt) grain with elevated As content, with pyrite (py) core and Au–Ag sulphide and acanthite (acn) droplets D) Grain separate of a rounded, concentric, Fe oxide/oxyhydroxide particle from brown "muds", with dense core and porous, concentric outer cortex, latter hosting pyromorphite (pym) spots. Both the core and the cortex have elevated Pb content E) In situ oxidised sulphide in calcite (cal) matrix of limestone from carbonate replacement mineralisation. Dense Fe oxide/oxyhydroxide core with Au–Ag sulphide and Ag–Hg sulphide droplets of around 5 µm. F) From brown "mud" a concentric goethite (gt) grain with spongy Au–Ag sulphide in the middle and electrum (el) droplets. The grain is hosted in smectite (smc) and Fe oxide/oxyhydroxide matrix with pyromorphite (pym) mineralisation. The composition of the Au–Ag sulphide phase was also analysed by WDS (*Table I*)

7. ábra. *Barna „sarak" és genetikailag kapcsolódó kőzetek ércszöveteit bemutató BSE SEM–EDS/WDS felvételek (20 kV gyorsítófeszültségen). A) Barna „sár" sávos belső mikroszerkezete, goethit- (gt) pszeudomorfózákban gazdag, agyagdomináns és törmelékes ásványokban gazdag részekkel; kvarc (q), K-földpát (kfs) és grosszulár (grs) jelenlétével. B) Barna „sár" minta szemcsés belső mikroszerkezete piromorfittal (pym). C) Szkarnból származó, ötszögletes, koncentrikus goethit- (gt) szemcse emelkedett As-tartalommal, pirit- (py) maggal, valamint Au–Ag-szulfid- és akantit- (acn) kiválásokkal. D) Barna „sárból" származó, lekerekített, koncentrikus, szeparált Fe-oxid/oxihidroxid szemcse tömör maggal és porózus, koncentrikus külső burokkal; ez utóbbi piromorfit- (pym) foltokat tartalmaz. Mind a mag, mind a burok emelkedett Pb-tartalmú. E) Mészkő kalcit- (cal) mátrixában helyben oxidálódott szulfidásvány karbonáthelyettesítéses ércesedésből. Tömör Fe-oxid/oxihidroxid mag, mintegy 5 µm-es Au–Ag-szulfid- és Ag–Hg-szulfid-kiválásokkal. F) Barna „sárból" származó koncentrikus goethit- (gt) szemcse, középső részén szivacsos Au–Ag-szulfiddal és elektrum- (el) kiválással. A szemcse szmektit- (smc) és Fe-oxid/oxihidroxid mátrixban helyezkedik el, piromorfit- (pym) ásványosodással. Az Au–Ag-szulfid fázis WDS-sel mért összetételét az* I. táblázat *mutatja*

Table I. Summary of S, Au and Ag WDS analysis of a Au-bearing grain from sample MD1908 in comparison to ideal petrovskaite and uytenbogaardtite mineral compositions. The measured Au-Ag sulphide is clearly different from the ideal uytenbogaardtite, because its Ag/Au atomic ratio is much lower than 3. The composition is closer to petrovskaite in terms of Au dominance, but it is still more Au-rich and Ag-poor than ideal AgAuS. Because the WDS analytical totals are low (83.00–88.08 wt%), the phase is best referred to as an Au-rich Ag-Au sulphide with petrovskaite-like composition, rather than as a confirmed petrovskaite

I. táblázat. *Az MD1908-as minta vizsgált aranyhordozó szemcséjének S-, Au- és Ag-tartalmára vonatkozó WDS-elemzések összefoglalása, összehasonlítva a petrovskaite és az uytenbogaardtite ideális ásványösszetételével. A mért Au-Ag-szulfid egyértelműen eltér az ideális uytenbogaardtite összetételétől, mivel Ag/Au atomaránya jóval kisebb 3-nál. Összetétele az Au-dominancia szempontjából közelebb áll a petrovskaite-éhoz, ugyanakkor az ideális AgAuS-hez képest még annál is Au-dúsabb és Ag-szegényebb. Mivel a WDS-elemzések tömegszázalékos összege alacsony (83,00-88,08 tömeg%), a fázist petrovskaite-szerű összetételű, Au-dús Ag-Au-szulfidként írjuk le, nem pedig bizonyítottan azonosított petrovskaite-ként*

Phase / composition	S a%	Ag a%	Au a%	Ag/Au atomic ratio	Empirical formula
Analysed Au–Ag sulphide (mean ± 1σ, n = 5)	39.38 ± 0.81	26.33 ± 1.44	34.30 ± 0.71	0.77	$Ag_{0.67}Au_{0.87}S$
Petrovskaite	33.33	33.33	33.33	1.00	AgAuS
Uytenbogaardtite	33.33	50.00	16.67	3.00	Ag_3AuS_2

occurs as 0.5–1 μm droplets in As-bearing goethite rims of pseudomorphs after pyrite.

Sample A182012 from the exploration trench BITR126, in the Korkan West-Bigar Hill limestone area, is a karst-infill material with 0.99 ppm Au. It is a brown clayish saprock with 1–2 mm white angular to subangular clasts. SEM–EDX/WDS mapping shows P- and As-bearing Fe oxyhydroxide pseudomorphs after pyrite (*Figure 8/B*) and 2–4 μm native gold hosted by goethite with low As content (*Figure 8/C*).

Sample MD1909 from drillhole BIDD019 at 127.3–127.4 m represents in-situ oxidised limestone right below the brown "muds", it contains 1.30 ppm Au and exhibits few-micrometre-sized Au–Ag–S and Ag–Hg–S mineralisation in its dense core. It is not clayey and is best treated as an oxidised carbonate replacement sample rather than a redeposited brown "mud" (*Figure 7/E*). Its relevance is that it links the karst-infill material to the in situ oxidised mineralisation of carbonate host rocks.

Marmorised limestones

Marmorised limestones are widespread in the Bigar area. Field mapping showed that the degree of marmorisation increases from north to south, towards the Potaj Čuka monzonite (*Figure 2*). Limestone passes into weak marble and then into coarse to very coarse crystalline marble; within the marble domain, calcite crystal size also increases toward the inferred heat source. Numerous outcrops were mapped in this area, although exposure is discontinuous because of soil cover, vegetation and karstification.

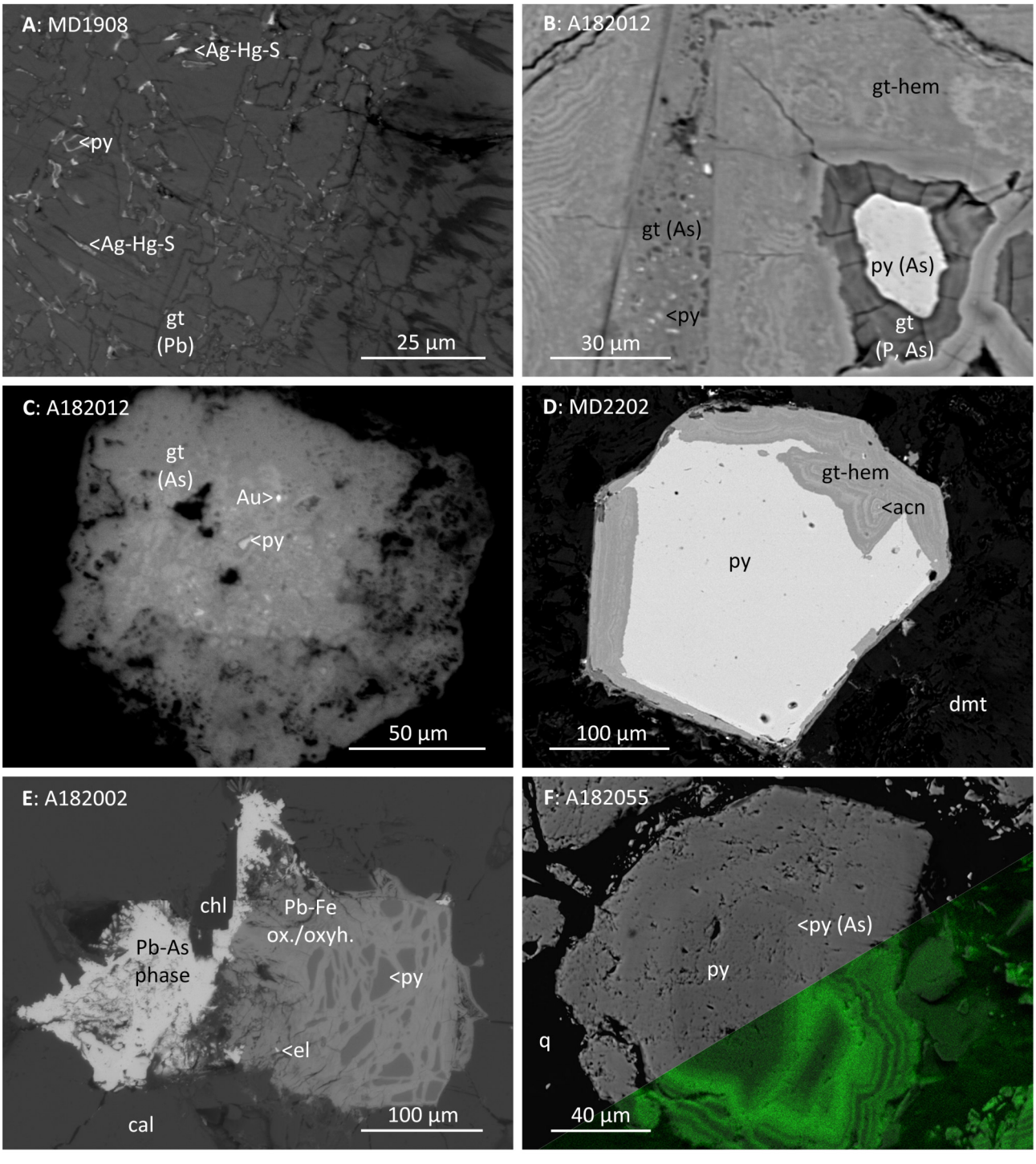
Macroscopically, the marble samples are white to light grey, commonly recrystallised, locally fractured and cut by rusty brown veinlets. Some samples contain disseminations of brown, grey and black cubes and spheres. Petrographically, the main mineral is coarse calcite, with ore minerals in intercrystalline spaces and thin veinlet networks. Fresh or partly preserved ore minerals include pyrite (*Figure 8/D; E*), galena , arsenopyrite and tetrahedrite-group minerals. Weathering products are dominated by Pb-rich Fe oxide/oxyhydroxide phases, with minor amounts of Sb, Zn, Cu and Mn and also include secondary Pb–As phases. Dissolution residue testing of carbonate material was conducted to concentrate the more resistant ore and oxide phases in the sample. A 100 g sub-sample of marble sample A182002 was subjected to dissolution in 10% HCl, leaving only 0.20 g of residue. The heavy, non-clay fraction, interpreted to contain Fe oxyhydroxide pseudomorph grains, weighed 0.07 g, equivalent to approximately 0.07 wt% of the original rock.

Sample A182002 is the most characteristic mineralised marble sample from the Bigar area, collected from the surface, about 250 m south of the high gold-grade brown "mud" sample taken from the BIDD019 drillhole. The bulk A182002 sample contains 0.14 ppm Au. SEM–EDS/WDS mapping showed electrum with approximately $Au_{0.75}Ag_{0.25}$ composition in a secondary Pb–Fe oxide/oxyhydroxide phase surrounding pyrite remnants (*Figure 8/E*). Acanthite is present farther surrounding the sulphide-bearing zones, where the Pb–Fe oxide/oxyhydroxide phase also shows elevated P content, while As is slightly elevated around pyrite relicts.

Skarns

Skarn-altered assemblages occur mainly near the contact between marmorised carbonate rocks and intrusive bodies in the Bigar area. They are less continuously exposed than the marble, but occur in several surface outcrops, trenches and drill-core intervals. Fresh or weakly

→ **Figure 8.** BSE images of SEM-EDS/WDS analyses (at an accelerating voltage of 20 kV) of the textures of brown "mud" ores and genetically related rocks. A) A grain from brown "mud": late Ag-Hg sulphide precipitation along fractures of Pb-rich Fe oxide/oxyhydroxide pseudomorphs after pyrite, often in the vicinity of residual pyrite. B) Brown "mud" sample from an exploration trench: in As-rich goethite (gt) matrix, dense goethite-hematite (gt-hem) cubes with As-rich pyrite (py) relicts. Around the relict pyrite less porous Fe oxyhydroxide rim with elevated P and As content is present. C) From brown "mud" a euhedral Fe oxide/oxyhydroxide grain with elevated As content, with pyrite (py) relicts and native gold (Au) droplets. D) Carbonate-replacement sample: idiomorphic pyrite (py) crystal from dolomitic (dmt) marble being replaced by alternating goethite-hematite (gt-hem) assemblage, containing acanthite (acn). E) Carbonate-replacement sample: in situ oxidised sulphide assemblage in marble (cal).



Secondary Pb–As phase and pyrite (py) are present with electrum (el) droplets. The pyrite is consumed by an unidentified Pb–Fe oxide/oxyhydroxide phase. Calcite shows weak signs of carbonate re-dissolution. F) Composite image of fresh, euhedral pyrite (py) crystals from the S1 sandstone unit of a sedimentary rock-hosted mineralisation: Slight difference of As content in pyrite on the BSE image (upper left) is well highlighted on WDS element mapping (lower right): distinct, concentric As-rich (green) bands are present

8. ábra. *Barna „sarak" és genetikailag kapcsolódó kőzetek ércszöveteit bemutató BSE SEM–EDS/WDS-felvételek (20 kV gyorsítófeszültségen). A) Barna „sár" szemcsepreparátumából: késői Ag–Hg-szulfid-kiválás a pirit utáni, Pb-dús Fe-oxid/oxihidroxid pszeudomorfózák repedései mentén, melyek közelében gyakran figyelhetőek meg relikt piritek. B) Barna „sár" kutatóárokból: As-dús goethit- (gt) mátrixban tömör goethit–hematit (gt-hem) kockák, As-dús pirit- (py) reliktumokkal. A relikt pirit körül kevésbé porózus, emelkedett P- és As-tartalmú Fe-oxihidroxid perem figyelhető meg. C) Barna „sárból" származó, idiomorf, emelkedett As-tartalmú Fe-oxid/oxihidroxid szemcse pirit- (py) reliktumokkal és termésarany- (Au) szemcsékkel. D) Karbonáthelyettesítéses ércminta: dolomitos márványból származó idiomorf pirit- (py) kristály, amelyet akantitot (acn) tartalmazó, váltakozó goethit–hematit (gt-hem) ásványegyüttes helyettesít. E) Karbonáthelyettesítéses ércminta: márványban helyben oxidálódott szulfidos ásványegyüttes. Másodlagos Pb–As fázis és pirit (py) figyelhető meg elektrum- (el) szemcsével. A piritet egy azonosítatlan Pb–Fe-oxid/oxihidroxid fázis emészti fel. A kalcit enyhe karbonát-visszaoldódási jegyeket mutat. F) Üledékes kőzetekhez kötött ércesedésű S1 homokkőből származó friss, idiomorf pirit- (py) kristályok kompozit képe. A pirit As-tartalmának BSE-képen (bal felső) megfigyelhető csekély különbségét a WDS-elemtérképen (jobb alsó) a koncentrikus, zöld színű sávok már jól mutatják*

weathered skarn and skarn-related calc-silicate samples are generally greenish grey, hard and mottled. They contain quartz, calcite, epidote, grossular, talc, hematite and other calc-silicate minerals. Fe sulphide relicts are found in Fe oxyhydroxide grains, in which locally galena droplets, Ag sulphide mineralisation and Pb–Zn-bearing Fe oxyhydroxide products are present. The ICP–MS-analysed skarn samples show a stronger Mn–Pb–Fe–Cd signature and locally contain elevated Ag and As, matching the observed Pb–Zn-bearing goethite, Mn–Pb-rich precipitates and Ag sulphide phases (*Supplementary Table S3a*).

Sample A182009 from exploration trench BITR112 at 20–22 m, is a greenish-grey to yellowish-brown hard skarn from the Bigar area with 1.59 ppm Au. No visible gold was observed in the analysed section, but microscopic-sized silver minerals are abundant. SEM–EDX mapping shows Fe sulphide relicts, probably pyrrhotite or pyrite, surrounded by Pb-, As- and Zn-bearing goethite and more compact hematite. Ag sulphide, most probably acanthite/argentite, occurs in vugs and veinlets of goethite-dominated parts. Later Pb–As–Zn–Mn precipitates occur along hematite lamellae and as irregular patches.

Sample A182008 from channel BICH109 at 26–28 m is a representative example of a weathered skarn sample in the vicinity of a brown "mud"-dominated area. It contains a pentagonal, concentrically-zoned goethite pseudomorph after pyrite, with a pyrite relict in the core (*Figure 7/C*). Au–Ag sulphides and acanthite occur as 0.5–1 μm blebs in the inner As-rich goethite part. Au and Ag form a vague zone around the relict pyrite core. Outwards, the grain exhibits a more compact hematite ring, then an As-rich, more porous outer rim of goethite. This is the most representative skarn-derived example of the same pyrite-to-goethite-to-Au-bearing oxide sequence seen in the brown muds.

Sandstones

To find out any possible relationship between the brown "muds" and the wider geological setting, eight S1 sandstone samples were also collected from three metallurgical drill cores of the Korkan area. The most important sample in relation to the brown "muds" is A182055 from the KODDMET003 drill hole, which is a transitional S1 sandstone with 1.08 ppm Au. SEM–WDX mapping showed well-developed As zoning in fresh pyrite (*Figure 8/F*). The pyrite crystals contain alternating As-rich and As-poor zones, but no visible Au was observed in them. This banded texture is important because it provides the best-preserved precursor for As-bearing Fe oxide/oxyhydroxide pseudomorphs observed in more oxidised samples. The Korkan S1 sandstone samples show variable Au contents with moderate As and locally elevated Sb–Tl, but without the strong Pb–Mn–Cd enrichment typical of the skarn-related or some karst-infill samples (*Supplementary Table S3a*).

No microscopic gold mineralisation was observed in any fresh pyrite of the above samples.

Discussion

Genetic model for Au-rich brown "mud" formation

The gold-rich brown "muds" occur on karstic marble surfaces exposed in exploration trenches and between marble units in drill core, including a 15.5 m drilled interval in BIDD019 (*Figures 3–4*). They are weakly consolidated, with locally banded or brecciated textures and generally with a carbonate-poor matrix. They are a heterogeneous mixture of clay, angular to subrounded Fe oxide/oxyhydroxide grains, carbonate fragments and detrital silicate minerals (*Figures 5–7*). Based on these field relationships and sedimentary features the brown "muds" are interpreted as karst-infill material.

Though there are documented pre-mineralisation karst cavities with breccia and siliciclastic fills at Bigar Hill (KNAAK et al. 2016), the studied brown "muds" are interpreted to record later weathering and reworking of already mineralised material. This interpretation is supported by the variably rounded, precious-metal-bearing Fe oxide/oxyhydroxide grains in the brown "muds", and comparable oxidised, partially oxidised and fresh grains of euhedral pyrite still enclosed in marble and skarn samples from the studied area. By weathering, the early mineralised karst infills could also have contributed to this material, and older cavities may have also been reused during redeposition.

The observed mineral phases and their textural relationships suggest that the studied samples can be arranged into a stepwise genetic sequence. To illustrate the inferred changes in redox and pH conditions at 25°C, a schematic composite Eh–pH diagram was constructed by compiling and simplifying mineral and aqueous-species fields from published diagrams (*Figure 9*). Because the source diagrams were calculated for different chemical systems, component activities and thermodynamic datasets, the resulting field relationships are used only qualitatively. The numbered trajectory represents the proposed genetic sequence derived from the observed mineral assemblages and textures, not a quantitatively modelled reaction path. The major steps are also summarised in a series of sketches to show their relationship to the host rocks and primary mineralisation (*Figure 10*).

The first stage involves primary sulphide formation under reducing conditions (Figures 9, 10/A). Primary sulphide mineralisation occurred in carbonate-replacement and skarn settings in the area (KNAAK et al. 2016), consistent with relict sulphides and their Fe oxide/oxyhydroxide replacement products in the studied marble and skarn samples (*Figures 7/C, 8D–E*). The sedimentary rock-hosted setting is represented by the mineralogical observations of PAČEVSKI (2012a, b) and ŽIVANOVIĆ (2019) from Bigar Hill and the well-developed As-zoned pyrite in sample A182055 from the S1 sandstone from Korkan (*Figure 8/F*). Although the bulk sample contains 1.08 ppm Au, there is no evidence

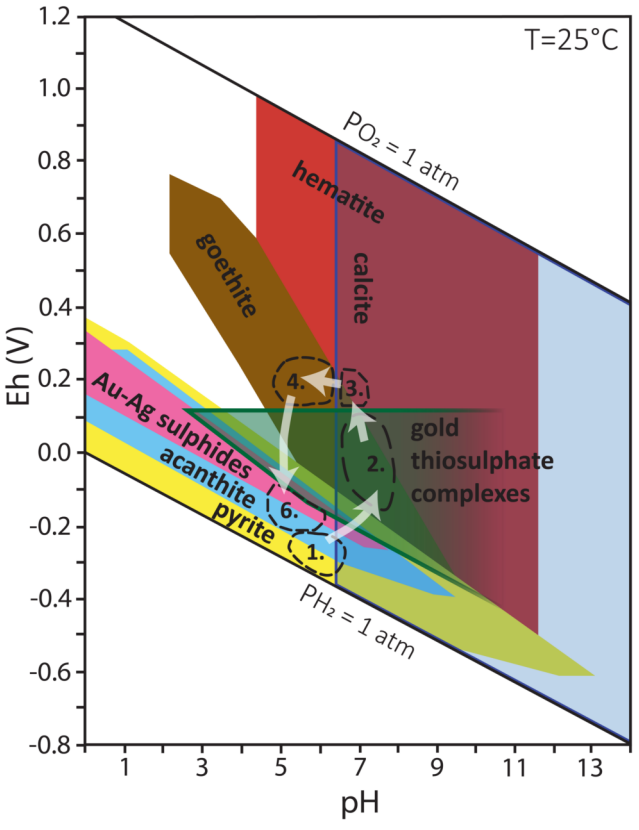


Figure 9. Schematic composite Eh–pH diagram illustrating the inferred supergene–karstic evolution of the Au–Ag-bearing mineral assemblage. Black, dashed areas correspond to genetic phases referred to in the discussion. Approximate stability fields of minerals and aqueous species were compiled and redrawn based on the following publications: Au–Ag–S phases: Savva et al. (2014); Fe oxides and oxyhydroxides: Brown (1971), Schachtschabel et al. (1989) and Takeno (2005); acanthite: Tuduri et al. (2011); pyrite: Barnes (1967); Au–thiosulphate complex: Craw et al. (2015) and Webster (1986), calcite: Brookins (1988)

9. ábra. *Az Au–Ag-tartalmú ásványegyüttes feltételezett szupergén–karsztos fejlődését szemléltető, sematikus, összetett Eh–pH diagram. A fekete, szaggatott vonallal jelzett tartományok a diszkusszióban részletezett genetikai fázisoknak felelnek meg. Az ásványok és oldott kémiai formák közelítő stabilitási mezőit az alábbi munkák alapján szerkesztettük újra: Au–Ag–S: Savva et al. (2014); Fe-oxidok és -oxihidroxidok: Brown (1971), Schachtschabel et al. (1989) és Takeno (2005); akantit: Tuduri et al. (2011); pirit: Barnes (1967); Au–tioszulfát-komplex: Craw et al. (2015) és Webster (1986); kalcit: Brookins (1988)*

of visible gold mineralisation. Therefore, gold is interpreted to be present mostly as invisible gold, either as structurally bound gold or as nanoscale native gold inclusions in As-rich pyrite. This interpretation is consistent with the known sandstone-hosted mineralisation at the Bigar Hill deposit referred to as a sedimentary rock-hosted gold mineralisation (Zimmerman et al. 2008, Knaak et al. 2016), where sulphidation of Fe-bearing minerals and ferroan carbonate cement formed pyrite that hosts invisible gold (Pačevski 2012a, b; Živanović 2019). In the present model, the As-bearing pyrite is regarded as the precursor of later Au-bearing Fe oxyhydroxide pseudomorphs. A comparable micrometre-scale process was documented in the Otago Schist gold deposits, where oxidation of Au-bearing pyrite and arsenopyrite produced Fe oxyhydroxide pseudomorphs and liberated or locally redeposited gold previously present as encapsulated microparticles or in solid solution within the sulphides (Craw et al. 2015).

The second stage is inferred to have begun with a relative fall in the groundwater table, possibly linked to post-mineralisation tectonic movements documented by Knaak et al. (2016), increasing Eh and exposing sulphides to meteoric waters, leading to their incipient oxidation. In the carbonate-rich environment of marble and limestone, acids generated by sulphide oxidation were buffered, so pH probably remained weakly acidic to near neutral (Lakin et al. 1974, Craw et al. 2015). Under these conditions, chemical weathering of pyrite produced thiosulphate ions, and the pyrite was progressively replaced by Fe oxide/oxyhydroxides (*Figures 8/D; 9; 10/B*).

By the third stage, oxidation advanced and the released thiosulphate ions were able to form complexes with the nanoscale Au and Ag content of pyrite grains under weakly oxidising conditions and at weakly acidic to near neutral pH (Webster 1986, Craw & Mackenzie 1992, Craw et al. 2015). Evidence of the latter can be seen on *Figure 8/E*, where the calcite host shows weak signs of carbonate re-dissolution around an oxidised sulphide phase. In an increasing Eh environment Au and Ag thiosulphate complexes become unstable and micrometre-sized native gold or electrum precipitates (*Figure 9*). The narrow stability field of Au and Ag thiosulphate complexes explains why gold remained close to its source pyrite, but changed its form from nanoscale invisible gold to visible micrometre-sized particles (*Figure 8/E*). Similar short-distance Au remobilisation by thiosulphate complexes was described by Stoffregen (1986), Castor & Sjoberg (1993) and Craw et al. (2015). Silver may have been transported slightly farther because it can remain soluble as thiosulphate complexes under moderately oxidising conditions (Webster 1986, Perera & Senanayake 2004). This interpretation is supported by the occurrence of Ag-bearing phases in a wider range of samples and textural positions than Au-bearing phases: acanthite and Au–Ag sulphides in weathered skarn (*Figure 7/C*); Au–Ag and Ag–Hg sulphides in an in situ oxidised carbonate-hosted sulphide assemblage (*Figure 7/E*); acanthite in a partially oxidised pyrite grain from dolomitic marble (*Figure 8/D*); and fracture-hosted Ag–Hg sulphides in redeposited karst-infill material (*Figures 7/D; 8/A*). This wider distribution is consistent with greater local mobility of Ag, although differences in the primary Ag abundance cannot be excluded.

The fourth stage involved karstification and the physical liberation of the Au-bearing Fe oxyhydroxide grains. Presumably, continued tectonic movements further increased the relative fall of the water-table and carbonate dissolution opened cavities and removed carbonate host material (*Figure 9*). This process separated ore-bearing Fe oxyhydroxide grains from the barren carbonate. In this sense, it acted as a natural combination of leaching and gravity concentration: carbonate was dissolved, whereas resistant goethite-hematite pseudomorphs, clay minerals, and heavy detrital grains remained unleached and could be physically liberated from their carbonate host rock (*Figure 10/C*).

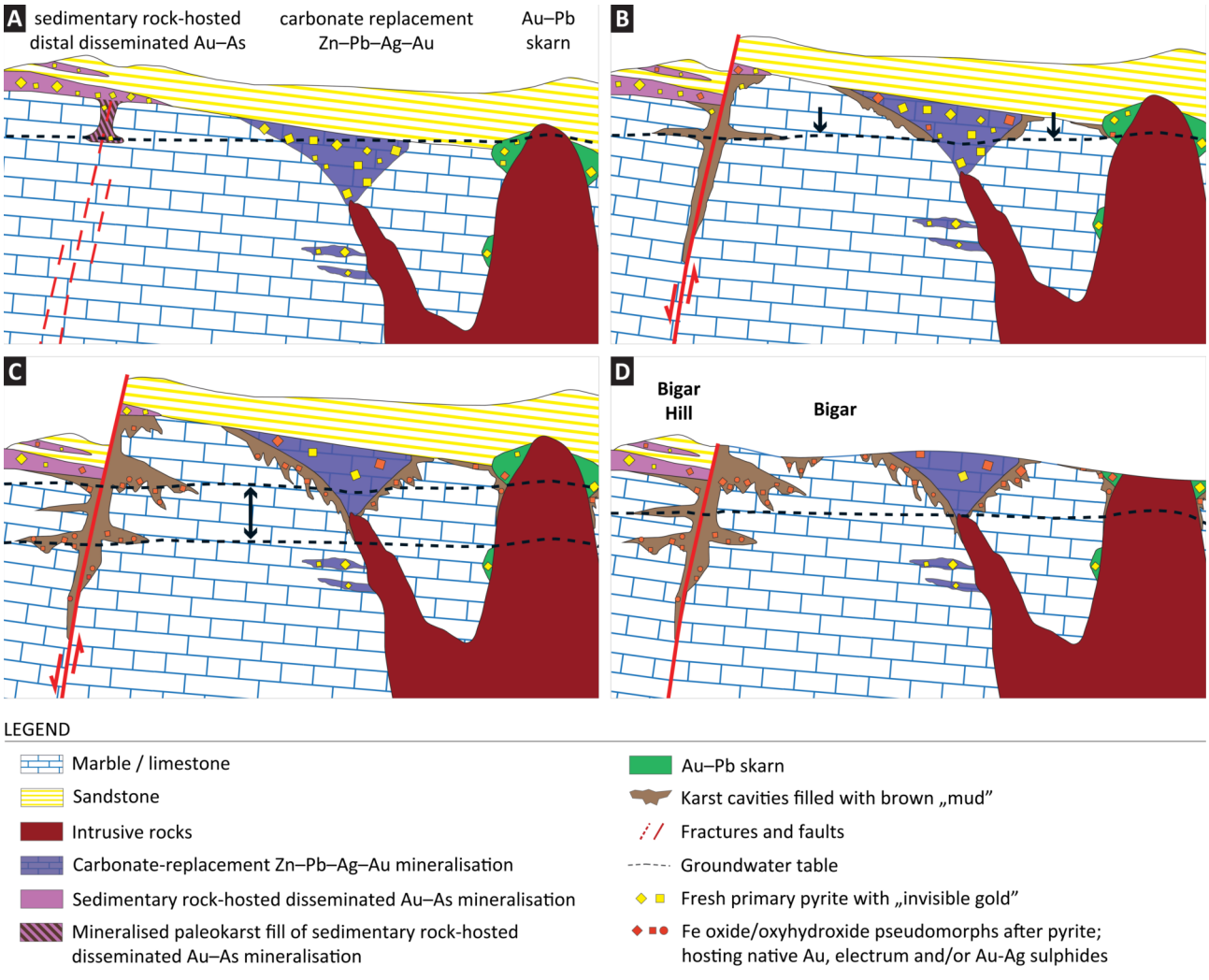


Figure 10. Schematic model of primary mineralisation and the proposed formation of the gold-rich brown "muds" in the Bigar area, Western Timok, Serbia. The arrangement of primary mineralisation types follows SILLITOE (2010), adapted to the local geological setting using KNAAK et al. (2016) and ŽIVANOVIĆ (2019). A) Primary skarn, carbonate-replacement and sedimentary rock-hosted mineralisation (including the primary mineralisation of early karst infills). In the sedimentary rock-hosted mineralisation gold is interpreted to occur mainly as "invisible" gold in As-bearing pyrite, either structurally bound or as submicrometre-sized native gold inclusions. B) Lowering of the groundwater table (possibly induced by tectonic movements) changed reducing conditions to oxidative, and the oxidation of primary sulphides commenced. The "invisible" gold content of the grains may have been remobilised locally by thiosulphate complexes and reprecipitated within individual grains as micrometre-sized native gold and electrum. C) Further karstification, liberation and physical reworking of gold-bearing, oxidised to partially oxidised grains, and their accumulation in karst cavities. Groundwater-table fluctuations may have promoted further Au–Ag redistribution and late Au–Ag sulphide precipitation under locally reducing conditions in the presence of dissolved sulphide. D) Erosion and exposure of mineralised carbonate rocks and brown karst infill, with the sedimentary rock-hosted gold mineralisation preserved in the downfaulted block at Bigar Hill. The model is schematic and not to scale

10. ábra. *Az elsődleges ércesedés és az aranyban gazdag barna „sár" feltételezett kialakulásának sematikus modellje a Bigar területen, Nyugat-Timokban, Szerbiában. Az elsődleges ércesedéstípusok térbeli megjelenése* SILLITOE *(2010) modelljét követi a helyi földtani viszonyokhoz igazítva* KNAAK *et al. (2016) és* ŽIVANOVIĆ *(2019) alapján. A) Elsődleges szkarn-, karbonáthelyettesítéses és üledékes kőzetekhez kötődő ércesedés, beleértve a korai karsztkitöltések elsődleges ércesedését is. Az üledékes kőzetekhez kötődő ércesedésben az arany főként „láthatatlan" formában, As-tartalmú piritben fordul elő: szerkezetileg kötött aranyként vagy szubmikrométeres termésarany-zárványokként. B) A feltételezetten tektonikai mozgások által előidézett talajvízszint-süllyedés elősegítette az elsődleges szulfidok reduktív közegből való kimozdulását így azok oxidációja megindulhatott. A szemcsék „láthatatlan" aranytartalma helyileg, tioszulfátkomplexek közvetítésével remobilizálódhatott, majd az egyes szemcséken belül mikrométeres termésaranyként és elektrumként vált ki újra. C) A karsztosodás folytatódása, az oxidált vagy részlegesen oxidált aranyhordozó szemcsék felszabadulása és fizikai áthalmozódása karsztüregekbe. A talajvízszint ingadozása elősegíthette az Au és Ag további átrendeződését, késői Au–Ag-szulfidok kiválását helyi reduktív körülmények között, oldott szulfid jelenlétében. D) Az erózió feltárta az ércesedett karbonátos kőzeteket és a barna karsztkitöltéseket, miközben a Bigar Hill vető mentén levetett tömbjében megőrződött az üledékes kőzetekhez kötődő aranyércesedés. A modell sematikus, nem méretarányos*

The fifth stage was physical transport, i.e. grain redeposition. The presence of both euhedral and subrounded to rounded Fe oxyhydroxide pseudomorphs after pyrite suggests different degrees of reworking within the karst system (*Figures 5; 7/D; 8/C*). Abrasion during transport generally makes grains more rounded (KRUMBEIN 1941), but transport distance cannot be estimated from grain shape alone. The different grain shapes may reflect several nearby mineralised source areas and different degrees or repeated episodes of transport and redeposition. Comparable gold-bearing oxidation products in nearby marble and skarn suggest a local source for at least part of the karst infill. Transport over tens to hundreds of metres is a plausible working hypothesis; comparable distances have been documented for transported gossans (VE-

LASCO et al. 2013). However, the available textures and field relationships do not establish a maximum transport distance.

The concentric Fe oxide/oxyhydroxide coatings were formed after the enclosed grain cores, but their mode of formation and timing relative to redeposition remain uncertain. The layer-parallel goethite-rich domains of the brown "mud" samples may represent precipitation during or after deposition of the material. Alternatively, they could reflect weathering of Fe-bearing layers in older sedimentary karst fills that had previously undergone hydrothermal mineralisation. The observed textures alone do not distinguish between these possibilities or establish the timing of these domains relative to the main mineralising event.

The sixth stage took place after the grains were redeposited into karst cavities that were probably periodically filled with water. Paleokarst and younger karst features are known from the area, and organic matter occurs in several local carbonate and fine-grained sedimentary units (KNAAK et al. 2016, ŽIVANOVIĆ 2019). Where water circulation was limited, oxygen consumption during organic matter degradation could have lowered Eh. Sulphate – produced during earlier sulphide oxidation – may have been reduced to dissolved sulphide species, as observed in other anoxic karst aquifers (APPELO & POSTMA 2005, GUO et al. 2021). Reaction with carbonate material would tend to buffer acidity, although neither Eh nor pH can be estimated from the available data. In the presence of reduced sulphide species native gold or electrum could be replaced by Au–Ag sulphides (*Figure 9*). Depending on the fineness (Au/Ag ratio) of gold, it can be replaced by uytenbogaardtite (Ag_3AuS_2), petrovskaite (AuAgS), and/or acanthite (Ag_2S) (SAVVA & PAL'YANOVA 2007, PAL'YANOVA et al. 2014). This process is well recorded in sample MD1908, where a spongy-looking, 30 μm sized Au–Ag sulphide occurs in the middle of an Fe oxyhydroxide aggregate, while few unconsumed 2–5 μm sized electrum droplets are still observed around it (*Figure 7/F*). SEM–WDX analyses of this grain indicate that the average empirical composition of the Au–Ag–S mineral phase is approximately $Ag_{0.67}Au_{0.87}S$ (*Table I*). This composition is closest to petrovskaite, but it is more Au-rich and Ag-poor than ideal AgAuS; therefore, the phase is best referred to as an Au-dominant Au–Ag sulphide. Precise mineral identification would require confirmation by crystallographic or Raman data.

Locally reducing conditions in the presence of dissolved sulphide species – such as H_2S and HS^- – may have facilitated the late precipitation of Ag sulphides and Ag–Hg sulphides within the karst system (YESARES et al. 2014, GUO et al. 2021). The studied materials contain acanthite, Ag–Hg sulphides, cinnabar, galena, sphalerite and pyrite as 1–5 μm-sized patches and blebs. Sample MD1908, a karst-infill drill core sample from the Bigar area records this late karst-related sulphide precipitation: abundant Ag–Hg sulphides occur along fractures within Fe oxide/oxyhydroxide pseudomorphs after pyrite and are commonly associated with relict pyrite (*Figure 8/A*). The pyrite core surrounded by a goethite–hematite replacement rim in *Figure 8/D* records a microscale oxidation front. Such core–rim textures develop during pyrite oxidation and replacement by Fe oxides/oxyhydroxides (RIMSTIDT & VAUGHAN 2003, TAIVALKOSKI et al. 2024). The occurrence of acanthite within the replacement rim, together with fracture-hosted Ag–Hg sulphides next to pyrite remnants in sample MD1908 (*Figure 8/A*), is consistent with local remobilisation and reprecipitation of Ag and Hg during supergene redox cycling, as described from other weathering profiles (YESARES et al. 2014). This textural relationship suggests that Ag and Hg – possibly remobilised from the weathering of primary sulphides – could precipitate at local redox-reaction fronts. Fluid-mediated reaction with incompletely oxidised pyrite may have promoted Ag–Hg sulphide precipitation and potentially supplied part of the sulphur, although the textures do not unequivocally demonstrate direct replacement of pyrite. These late precipitates show that the karst cavities were not merely passive sediment traps, but chemically active environments in which metals were remobilised and reprecipitated.

In some studied grains, Au–Ag sulphides or acanthite occur in dense inner domains, but are not observed in the outer, more porous Fe oxyhydroxide parts (*Figure 7/C, D, E*). Oxidation progressing from grain boundaries and fractures could have left parts of the inner domains less altered; such short-range Au mobilisation during sulphide oxidation has been described in comparable settings (CRAW et al. 2015). This subsequent weathering may have involved changes in redox conditions, possibly influenced by fluctuations in the paleo-water table. Although this phenomenon is not documented from the locality in the literature, current annual water-table fluctuations are known to be as high as 15 m at Bigar Hill (BLAHO et al. 2024), and it is inferred that these fluctuations could have been present earlier as well. Changes in the paleo-water table are one possible cause for redox fluctuations, as documented in other supergene deposits (YESARES et al. 2014). A fall in the water table could have increased oxygen access to the karst infill, raising Eh and promoting sulphide oxidation and Fe oxyhydroxide formation (RIMSTIDT & VAUGHAN 2003, Craw et al. 2015). Acidity generated by these reactions could have been partly neutralised by carbonate dissolution, limiting the decrease in pH (YESARES et al. 2014). Under near neutral to mildly alkaline conditions, thiosulphate could have promoted Au and Ag mobilisation by forming soluble complexes (CRAW et al. 2015). These processes remain hypothetical here, as the available data do not constrain the actual Eh, pH or dissolved sulphur species.

Overall, the studied brown "muds" are interpreted as composite, gold-bearing supergene karst infills. Their Fe-rich component is consistent with the oxicrete-(Fe) category of DILL et al. (2013) and occurs together with clay, detrital grains and later mineral precipitates. Their gold enrichment cannot be explained by one process alone. The proposed sequence began with carbonate-buffered oxidation of primary As-bearing pyrite containing invisible gold. Au and Ag were then remobilised over short distances, probably as thiosulphate complexes, and precipitated as micrometre-sized native gold and/or electrum within Fe oxyhydroxides. Karstification subsequently liberated the gold-bearing grains, which

were transported and redeposited in cavities. Later changes in redox conditions may have caused the formation and the subsequent partial removal of Au–Ag sulphides. Erosion exposed the mineralised carbonate rocks, and the brown "mud" karst infills in the Bigar area, while sedimentary rock-hosted gold mineralisation was preserved in the downfaulted block at Bigar Hill (*Figure 10/D*).

Implications and uncertainties

The bonanza gold grades within certain brown "muds" can be explained by the combination of chemical and physical concentration. First, oxidation and subsequent karst-related reactions converted invisible gold within pyrite into visible, micrometre-sized native gold, electrum and Au–Ag sulphides. Second, carbonate dissolution removed substantial volumes of barren host rock. Third, resistant goethite-hematite pseudomorphs after pyrite were physically concentrated in karstic traps. Consequently, karst infills like sample MD1908 reach 11.77 ppm Au, whereas the nearby in situ oxidised marble (sample A182002) a few hundred meters away contains only 0.14 ppm Au.

Regional intrusions formed at about 84–78 Ma (KNAAK et al. 2016), while hydrothermal illite ages suggest gold mineralisation at Bigar Hill at around 79 ± 3 Ma (ŽIVANOVIĆ 2019). The Potaj Čuka monzonite may have supplied heat, but its link to the mineralisation in the studied marble and skarn remains uncertain. Primary sulphides are possible sources of Fe, As, Au and Ag, while polymetallic marble and skarn assemblages may have contributed Pb, Zn and Mn. The primary Hg source is unknown. The recently described Čoka Rakita and Dumitru Potok deposits provide regional examples of such mineralisation, but are not demonstrated sources of the studied "muds".

For exploration, this means that brown "muds" should not be treated simply as fault gouge or residual clay. The most prospective material is expected where carbonate rocks, sulphide-bearing marble or skarn, karstification and structural pathways overlap. Key textural and geochemical indicators include As-bearing goethite, Pb-rich Fe oxyhydroxides, Mn–Pb oxyhydroxides, clay-rich karst infills and rounded goethite-hematite pseudomorphs. Furthermore, this model also suggests that high-grade oxide gold may occur away from the primary sulphide footprint, but still within short transport distance of several hundred metres from the sulphide sources.

Future exploration could combine targeted geochemical sampling with high resolution electrical resistivity tomography to help delineate low resistivity clay-rich karst infills from high resistivity carbonate rocks (PARK et al. 2009, CHENG et al. 2019). Lidar-derived terrain models could help identify surface karst depressions in forested areas (KOBAL et al. 2014), while multispectral imagery could help map exposed iron-rich weathering products (GE et al. 2020). These methods would require local testing and geological verification, and the gold content of identified targets would need to be established by sampling and assays.

Several uncertainties remain. The primary gold source is not fully constrained. As-rich pyrite in S1/S2 sandstone provides a regional analogue (ŽIVANOVIĆ 2019), while mineralised marble and skarn are also possible source rocks. Pyrite is reported from both carbonate-replacement and skarn assemblages in the western Timok area (KNAAK et al. 2016). In our marble sample A182002, electrum occurs in secondary Pb–Fe oxides/oxyhydroxides surrounding relict pyrite (*Figure 8/E*). In the weathered skarn sample A182008, Au–Ag sulphides occur in a goethite pseudomorph with a preserved pyrite core (*Figure 7/C*). These observations suggest that mineralised marble and skarn may have contributed gold-bearing material to the karst infills, although the original gold content of their pyrite remains uncertain. Additionally, the precise Eh–pH thresholds, sulphur sources and duration of the reduced karst stages lack direct measurements. The timing of uplift, oxidation, karstification and redeposition is only relatively constrained. Finally, the submicrometre-scale of gold-bearing phases limits SEM-EDX identification, especially for Au–Ag sulphides, Ag–Hg phases and phases prone to elemental overlaps.

Conclusions

This study extends earlier regional work by documenting the Au-bearing phases, their host grains and the internal texture of the brown karst infills of the Bigar area. The studied material contains pyrite-derived Fe oxide/oxyhydroxide pseudomorphs mixed with clay-rich domains, detrital grains and later mineral precipitates. The occurrence of angular to rounded pseudomorphs, concentric goethite–clay coatings, and layer-parallel Fe-rich precipitates supports a composite origin involving both redeposition and mineral formation within the infill.

The mineralogical observations show that native gold, electrum and Au–Ag sulphides occur within Fe oxide/oxyhydroxide grains. Acanthite and Ag–Hg sulphides are also present. The analysed Au–Ag sulphide has a petrovskaite-like composition, but its mineral identity remains unconfirmed. Dense inner domains containing precious-metal phases, porous outer rims, and sulphide-bearing fractures record differences in alteration within individual grains. These relationships provide evidence for a more complex history than a single stage of sulphide oxidation.

Size-fraction analyses provide additional evidence for the importance of the coarser gold-bearing grains. In the studied MD1908 subsample, the 63–125 μm fraction contained 16.11 ppm Au, compared with 2.80 ppm Au in the <32 μm fraction. Together with the microscopic observations, these results support the role of the coarser Fe oxide/oxyhydroxide pseudomorphs as important Au carriers in this sample.

The observations support a genetic model combining sulphide oxidation, Au–Ag redistribution, carbonate dissolution and physical concentration of resistant gold-bearing grains in karst cavities. Thiosulphate-assisted transport and later sulphide formation under locally reducing conditions

are inferred parts of this model. Electrum in the nearby oxidised marble provides a possible local source analogue, but the relative contributions of sandstone-hosted, carbonate-replacement and skarn-related mineralisation remain uncertain. A contribution from weathered, previously mineralised paleokarst fills also cannot be excluded.

For exploration, the results identify gold-bearing Fe oxide/oxyhydroxide grains and their textural relationships as useful features to examine in brown, clay-rich karst infills. Such material raises special attention where mineralised carbonate rocks or skarns occur close to karst cavities and structural pathways. The main contribution of this study is the evidence that the studied brown "muds" contain reworked gold-bearing weathering products, with textures suggesting further local Au–Ag redistribution. Carbonate dissolution and physical concentration of these grains may produce shallow, gold-rich karst fills that merit exploration.

Acknowledgements

The authors gratefully acknowledge Avala Resources Ltd. and its successor, DPM Metals, for granting access to the study area and providing the opportunity to collect the samples used in this research. We also thank Dragana Davidović, the exploration manager at the time of the 2014 and 2017-2018 studies, as well as the geologists, field staff and other colleagues, for their assistance and logistical support during fieldwork and sampling, especially Dragan Mirošević. Special thanks are extended to Zsolt Bendő, Tamás Váczi, Norbert Zajzon, Máté Zsigmond Leskó, László Aradi and George Daher for their contribution to the analytical work and for carrying out the mineralogical and microanalytical measurements that supported this study. We thank Matthias Knaak and an anonymous reviewer for their careful reading of the manuscript and constructive comments, which helped improve its clarity and scientific content. We also thank Gina Lukoczki for her careful language editing and helpful suggestions on terminology.

References – Irodalom

Appelo, C. A. J. & Postma, D. 2005: *Geochemistry, Groundwater and Pollution*. – 2nd edition, CRC Press/Balkema, Leiden, 649 p. https://doi.org/10.1201/9781439833544

Barnes, H. L. (ed.) 1967: *Geochemistry of Hydrothermal Ore Deposits*. – Holt, Rinehart and Winston, New York, xvi, 670 p.

Blaho, S., Gagnon, D., Leahy, K., Locatelli, M., Morrison, D. N., O'Connor, M., Pavlović, N., Sellars, E. & Vasquez, L. 2024: *NI 43-101 Technical Report, Preliminary Economic Assessment, Čoka Rakita Project, Eastern Serbia.* – 385 p.

Brookins, D. G. 1988: *Eh-pH Diagrams for Geochemistry*. – Springer-Verlag, Berlin–Heidelberg–New York, 176 p. https://doi.org/10.1007/978-3-642-73093-1.

Brown, J. B. 1971: Jarosite–goethite stabilities at 25 °C, 1 atm. – *Mineralium Deposita* **6/3,** 245–252. https://doi.org/10.1007/BF00208032.

Castor, S. B. & Sjoberg, J. J. 1993: Uytenbogaardtite, Ag_3AuS_2, in the Bullfrog mining district, Nevada. – *The Canadian Mineralogist* **31/1,** 89–98.

Cheng, Q., Chen, X., Tao, M. & Binley, A. 2019: Characterization of karst structures using quasi-3D electrical resistivity tomography. – *Environmental Earth Sciences* **78,** 285. https://doi.org/10.1007/s12665-019-8284-2

Cline, J. S., Hofstra, A. H., Muntean, J. L., Tosdal, R. M. & Hickey, K. A. 2005: Carlin-type gold deposits in Nevada: Critical geologic characteristics and viable models. – In: Hedenquist, J. W., Thompson, J. F. H., Goldfarb, R. J. & Richards, J. P. (eds): *Economic Geology One Hundredth Anniversary Volume*. Society of Economic Geologists, Littleton, 451–484. https://doi.org/10.5382/AV100.15

Craw, D. & MacKenzie, D. J. 1992: Near-surface secondary gold mobility and grain-size enhancement, Barewood Mine, east Otago, New Zealand. – *New Zealand Journal of Geology and Geophysics* **35/2,** 151–156. https://doi.org/10.1080/00288306.1992.9514509

Craw, D., MacKenzie, D. & Grieve, P. 2015: Supergene gold mobility in orogenic gold deposits, Otago Schist, New Zealand. – *New Zealand Journal of Geology and Geophysics* **58/2,** 123–136. https://doi.org/10.1080/00288306.2014.997746

De Weerdt, P., Ibrango, S., Gagnon, D., Liskovych, V., Bisaillon, C., Overall, R., Leahy, K., Ritchie, D., Vasquez, L. & White, G. 2021: *NI 43-101 Technical Report – Timok Project Pre-Feasibility Study, Žagubica, Serbia.* Prepared for Dundee Precious Metals Inc., effective date 23 February 2021, report date 30 March 2021 – DRA Americas Inc., 492 p.

Dill, H. G., Weber, B. & Botz, R. 2013: Metalliferous duricrusts ("orecretes") – markers of weathering: A mineralogical and climatic-geomorphological approach to supergene Pb-Zn-Cu-Sb-P mineralisation on different parent materials. – *Neues Jahrbuch für Mineralogie – Abhandlungen* **190/2,** 123–195. https://doi.org/10.1127/0077-7757/2013/0235

DPM Metals 2026: *Technical Report on Mineral Resource Estimate for Dumitru Potok, Frasen and Rakita North Prospects, Eastern Serbia*. – 241 p.

Ge, W., Cheng, Q., Jing, L., Wang, F., Zhao, M. & Ding, H. 2020: Assessment of the capability of Sentinel-2 imagery for iron-bearing minerals mapping: A case study in the Cuprite area, Nevada. – *Remote Sensing* **12/18,** 3028. https://doi.org/10.3390/rs12183028

Guo, F., Jiang, G. & Liu, F. 2021: Biological sulfate reduction in an epigene karst aquifer and its impact on cave environment. – *Journal of Hydrology* **602**. https://doi.org/10.1016/j.jhydrol.2021.126804

Heinrich, C. A. & Neubauer, F. 2002: Cu–Au–Pb–Zn–Ag metallogeny of the Alpine–Balkan–Carpathian–Dinaride geodynamic province. – *Mineralium Deposita* **37,** 533–540. https://doi.org/10.1007/s00126-002-0271-x

HOFSTRA, A. H. & CLINE, J. S. 2000: Characteristics and models for Carlin-type gold deposits. – In: HAGEMANN, S. G. & BROWN, P. E. (eds): *Gold in 2000*. Reviews in Economic Geology 13, Society of Economic Geologists, 163–220. https://doi.org/10.5382/Rev.13.05.

IVASCANU, P. 2024: Čoka Rakita: discovery & accelerated exploration of a new high-grade gold skarn deposit in Serbia. – *Proceedings of PDAC 2024 (Western Tethyan Session)*, Toronto, Canada.

JANKOVIĆ, S. 1997: The Carpatho-Balkanides and adjacent area: a sector of the Tethyan Eurasian metallogenic belt. – *Mineralium Deposita* **32**, 426–433. https://doi.org/10.1007/s001260050110

KNAAK, M., MÁRTON, I., TOSDAL, R., VAN DER TOORN, J., DAVIDOVIĆ, D., STRMBANOVIĆ, I., ZDRAVKOVIĆ, M., ŽIVANOVIĆ, J. & HASSON, S. 2016: Geologic Setting and Tectonic Evolution of Porphyry Cu-Au, Polymetallic Replacement, and Sedimentary Rock-Hosted Au Deposits in the Northwestern Area of the Timok Magmatic Complex, Serbia. – In: RICHARDS, J. P. (ed.): *Tectonics and Metallogeny of the Tethyan Orogenic Belt*. Society of Economic Geologists Special Publication **19,** 1–28. https://doi.org/10.5382/SP.19.01

KOBAL, M., BERTONCELJ, I., PIROTTI, F. & KUTNAR, L. 2014: Lidar processing for defining sinkhole characteristics under dense forest cover: A case study in the Dinaric Mountains. – *The International Archives of the Photogrammetry, Remote Sensing and Spatial Information Sciences* **XL-7,** 113–118. https://doi.org/10.5194/isprsarchives-XL-7-113-2014

KOLB, M., VON QUADT, A., PEYTCHEVA, I., HEINRICH, C. A., FOWLER, S. J. & CVETKOVIĆ, V. 2013: Adakite-like and normal arc magmas: Distinct fractionation paths in the eastern Serbian segment of the Balkan-Carpathian Arc. – *Journal of Petrology* **54/3,** 421–451. https://doi.org/10.1093/petrology/egs072

KRUMBEIN, W. C. 1941: The effects of abrasion on the size, shape and roundness of rock fragments. – *The Journal of Geology* **49/5,** 482–520, https://doi.org/10.1086/624985

LAKIN, H. W., CURTIN, G. C. & HUBERT, A. E. 1974: *Geochemistry of gold in the weathering cycle. – U.S. Geological Survey Bulletin* **1330,** vi, 80 p. https://doi.org/10.3133/b1330.

MAGYAR, L. M. 2014: *The mineralogical characteristics and origin of secondary gold accumulation in brown clays from Bigar prospect, Western Timok, Serbia.* – MSc thesis, Eötvös Loránd University, Department of Mineralogy, Budapest, 90 p.

MAGYAR, L. M. 2018: *Petrographic study of gold-rich oxide ore materials (and related rocks) from Timok NW drill cores and from the surface. Summary and interpretation of results, plus additional element maps by EMPA-WDS and EMPA-EDS methods.* – Dundee Precious Metals, internal technical report, Budapest, 76 p.

MÁRTON, I., KOUZMANOV, K., GROZA, N. & ZDRAVKOVIĆ, M. 2026: Geological transect through the Apuseni Mts. – Banat – Timok: Late Cretaceous magmatism and metal endowment. – In: DRĂGUȘANU, S., PLEȘ, G. & TĂMAȘ, C. G. (eds): *XXIII International Congress of the Carpathian-Balkan Geological Association CBGA 2026. Field Trips Guide Volume.* Presa Universitară Clujeană, Cluj-Napoca, 4–32.

MILIĆ, V., SUZIĆ, I., ŽIVANOVIĆ, J., ZDRAVKOVIĆ, M., MÁRTON, I., KRUMOV, I., GROZA, N., MILOŠEVIĆ, D., STRMBANOVIĆ, I., KOTLAJIĆ, B., KOTLAJIĆ, L., DROBNJAK, D., ZEKOVIĆ, A., MITIĆ, T., DUKIĆ-MIJUCIĆ, O., KITANOVIĆ, V., JANJIĆ, S., SUŠIĆ, D., KOVAČEVIĆ, V., ŠESTAK, A., METODIEV, S. & KUNCHEV, K. 2026: *Dumitru Potok Cu-Au Porphyry-Skarn Mineralization System within the Timok Magmatic Complex, Eastern Serbia*. – 19th Congress of Geologists of Serbia, organized by the Serbian Geological Society.

MUNTEAN, J. L., CLINE, J. S., SIMON, A. C. & LONGO, A. A. 2011: Magmatic-hydrothermal origin of Nevada's Carlin-type gold deposits. – *Nature Geoscience* **4,** 122–127. https://doi.org/10.1038/ngeo1064

PAČEVSKI, A. 2012a: *Mineralization in the Korkan and Bigar Hill areas: Final conclusions and discussion.* – Avala Resources Ltd., internal report, 9 p.

PAČEVSKI, A. 2012b: *Mineralogical study of the 13 samples from the Bigar Hill area.* – Avala Resources Ltd., internal report, 20 p.

PAL'YANOVA, G. A., KARMANOV, N. S. & SAVVA, N. E. 2014: Sulfidation of native gold. – *American Mineralogist* **99/5–6,** 1095–1103. https://doi.org/10.2138/am.2014.4677

PARK, S., KIM, C., SON, J.-S., YI, M.-J. & KIM, J.-H. 2009: Detection of cavities in a karst area by means of a 3D electrical resistivity technique. – *Exploration Geophysics* **40/1,** 27–32. https://doi.org/10.1071/EG08114

PERERA, W. N. & SENANAYAKE, G. 2004: The ammine, thiosulfato, and mixed ammine/thiosulfato complexes of silver(I) and gold(I). – *Inorganic Chemistry* **43/10,** 3048–3056. https://doi.org/10.1021/ic035301z

RADTKE, A. S., RYE, R. O. & DICKSON, F. W. 1980: Geology and stable isotope studies of the Carlin gold deposit, Nevada. – *Economic Geology* **75/5,** 641–672. https://doi.org/10.2113/gsecongeo.75.5.641

RIMSTIDT, J. D. & VAUGHAN, D. J. 2003: Pyrite oxidation: A state-of-the-art assessment of the reaction mechanism. – *Geochimica et Cosmochimica Acta* **67/5,** 873–880. https://doi.org/10.1016/S0016-7037(02)01165-1

SAVVA, N. E. & PAL'YANOVA, G. A. 2007: Genesis of gold and silver sulfides at the Ulakhan deposit, northeastern Russia. – *Russian Geology and Geophysics* **48/10,** 799–810. https://doi.org/10.1016/j.rgg.2007.09.006

SAVVA, N. E., PAL'YANOVA, G. A. & KOLOVA, E. E. 2014: Gold and silver minerals and conditions of their formation at the Dorozhnoye deposit, Magadan Region, Russia. – *Natural Resources* **5/9,** 478–495. https://doi.org/10.4236/nr.2014.59044.

SCHACHTSCHABEL, P., BLUME, H.-P., BRÜMMER, G., HARTGE, K. H. & SCHWERTMANN, U. 1989: *Scheffer/Schachtschabel: Lehrbuch der Bodenkunde*. 12., neu bearbeitete Auflage. – Ferdinand Enke Verlag, Stuttgart, 491 p.

SILLITOE, R. H. 2010: Porphyry Copper Systems. – *Economic Geology* **105/1,** 3–41. https://doi.org/10.2113/gsecongeo.105.1.3

STOFFREGEN, R. E. 1986: Observations on the behavior of gold during supergene oxidation at Summitville, Colorado, U.S.A., and implications for electrum stability in the weathering environment. – *Applied Geochemistry* **1/5,** 549–558. https://doi.org/10.1016/0883-2927(86)90062-4

TAIVALKOSKI, A., RANTA, J.-P., SARALA, P., MOILANEN, M., NIKKOLA, P. & SOUKKA, T. 2024: Pyrite–goethite alteration in supergene oxidation processes in till: Elemental distribution and evaluation of goethite usability as a fingerprinting tool for vectoring mineral deposits. – *Minerals* **14/7,** 668. https://doi.org/10.3390/min14070668

TAKENO, N. 2005: *Atlas of Eh-pH Diagrams: Intercomparison of Thermodynamic Databases*. – Geological Survey of Japan Open File Report 419, Geological Survey of Japan, AIST, 287 p.

Tuduri, J., Pourret, O., Chauvet, A., Barbanson, L., Gaouzi, A. & Ennaciri, A. 2011: Rare earth elements as proxies of supergene alteration processes from the giant Imiter silver deposit, Morocco. – In: Reich, M., Barra, F., Tornos, F. & Campos, E. (eds): *Let's Talk Ore Deposits. Proceedings of the Eleventh Biennial SGA Meeting.* Ediciones Universidad Católica del Norte, Antofagasta, Chile, 982 p.

Yesares, L., Sáez, R., Nieto, J. M., Ruiz de Almodóvar, G. & Cooper, S. 2014: Supergene enrichment of precious metals by natural amalgamation in the Las Cruces weathering profile (Iberian Pyrite Belt, SW Spain). – *Ore Geology Reviews* **58,** 14–26. https://doi.org/10.1016/j.oregeorev.2013.10.004

van der Toorn, J., Davidović, D., Hadjieva, N., Strmbanović, I., Márton, I., Knaak, M., Tosdal, R. M., Davis, B. & Hasson, S. 2013: A new sedimentary rock-hosted gold belt in eastern Serbia. – *12th Biennial SGA Meeting, Proceedings* **2,** 691–694.

Velasco, F., Herrero, J. M., Suárez, S., Yusta, I., Alvaro, A. & Tornos, F. 2013: Supergene features and evolution of gossans capping massive sulphide deposits in the Iberian Pyrite Belt. – *Ore Geology Reviews* **53,** 181–203. https://doi.org/10.1016/j.oregeorev.2013.01.008

Webster, J. G. 1986: The solubility of gold and silver in the system Au–Ag–S–O_2–H_2O at 25 °C and 1 atmosphere. – *Geochimica et Cosmochimica Acta* **50/9,** 1837–1845. https://doi.org/10.1016/0016-7037(86)90242-5.

Zdravković, M., Davidović, D., Živanović, J., Strmbanović, I., Groza, N., Milošević, D., Dukić-Mijucić, O., Janjić, S., Šestak, A., Milić, V., Drobnjak, D., Kotlajić, B., Kitanović, V., Mihajlović, J., Novicić, N., Mitić, T., Suzić, I., Ivascanu, P., Kunchev, K., Metodiev, S., Krumov, I. & Márton, I. 2024: New Genetic Type of Gold Deposit for Timok, Serbia: The High-Grade Gold Skarn Mineralization at Čoka Rakita Project. – *Proceedings of Society of Economic Geologists Annual Conference* (SEG 2024), Windhoek, Namibia.

Zimmerman, A., Stein, H. J., Hannah, J. L., Koželj, D., Bogdanov, K. & Berza, T. 2008: Tectonic configuration of the Apuseni–Banat–Timok–Srednogorie belt, Balkans–South Carpathians, constrained by high precision Re–Os molybdenite ages. – *Mineralium Deposita* **43,** 1–21. https://doi.org/10.1007/s00126-007-0149-z

Živanović, J. 2019: *Structural, stratigraphic and temporal constraints of gold mineralization in the Bigar Hill deposit, Timok region, Serbia*. – MSc thesis, University of British Columbia, Vancouver, 207 p.

Živanović, J., Davidović, D., Zdravković, M., Groza, N., Strmbanović, I., Milošević, D., Dukić-Mijucić, O., Janjić, S., Šestak, A., Milić, V., Drobnjak, D., Kotlajić, B., Kitanović, V., Mihajlović, J., Novicić, N., Mitić, T., Suzić, I., Metodiev, S., Kunchev, K., Kouzmanov, K., Pačevski, A., Ivascanu, P. & Márton, I. 2024: Hydrothermal Alteration and Mineralization Footprint of the Čoka Rakita High Grade Gold Skarn Deposit, Timok, Serbia. – *Proceedings of Society of Economic Geologists Annual Conference* (SEG 2024), Windhoek, Namibia.

Manuscript received: 2026/07/29

Digital Supplementary Tables

Table S1. Original samples and sampling locations
S1. táblázat. *Alapminták és mintavételi helyek*

Table S2. Investigated specimens, separated fractions and analytical methods
S2. táblázat. *Vizsgálati tételek, szeparált frakciók és alkalmazott módszerek*

Table S3a, b, c, d. Chemical analytical results
S3a, b, c, d. táblázat. *Kémiai elemzési eredmények*